Physics of Plasmas

RESEARCH ARTICLE | MARCH 04 2025

Magnetized liner inertial fusion platform development to assess performance scaling with drive parameters

M. R. Gomez ; S. A. Slutz ; C. A. Jennings; A. J. Harvey-Thompson ; M. R. Weis ; W. E. Lewis ; B. T. Hutsel ; D. C. Lamppa ; M. Geissel ; J. A. Crabtree; T. J. Awe ; D. A. Yager-Elorriaga ; D. E. Ruiz ; C. Aragon ; K. A. Benavidez; G. A. Chandler ; S. W. Cordaro ; J. R. Fein ; E. S. Field ; S. B. Hansen ; P. F. Knapp; J. Jackson ; R. J. Kaye ; M. Lowinske; L. M. Lucero ; C. E. Myers ; M. A. Mangan ; O. M. Mannion ; B. Norris; R. R. Paguio ; L. Perea; A. J. Porwitzky ; P. K. Rambo ; G. K. Robertson; D. C. Rovang ; F. Sanchez; M. E. Savage; M.-A. Schaeuble ; G. A. Shipley ; J. E. Shores; G. E. Smith; I. C. Smith; C. S. Speas; J. Taylor ; K. Tomlinson; K. A. Whittemore; J. M. Woolstrum ; E. P. Yu ; D. J. Ampleford ; K. Beckwith ; M. E. Cuneo ; E. C. Harding ; M. C. Jones ; R. D. McBride ; K. J. Peterson ; J. L. Porter ; G. A. Rochau ; J. Schwarz ; D. B. Sinars

Phys. Plasmas 32, 032702 (2025)
https://doi.org/10.1063/5.0253541

Physics of Plasmas ARTICLE pubs.aip.org/aip/pop

Magnetized liner inertial fusion platform development to assess performance scaling with drive parameters

Cite as: Phys. Plasmas **32**, 032702 (2025); doi: 10.1063/5.0253541
Submitted: 17 December 2024 · Accepted: 9 February 2025 ·
Published Online: 4 March 2025

View Online Export Citation CrossMark

M. R. Gomez,[1,a] S. A. Slutz,[1] C. A. Jennings,[1] A. J. Harvey-Thompson,[1] M. R. Weis,[1] W. E. Lewis,[1] B. T. Hutsel,[1] D. C. Lamppa,[1] M. Geissel,[1] J. A. Crabtree,[1] T. J. Awe,[1] D. A. Yager-Elorriaga,[1] D. E. Ruiz,[1] C. Aragon,[1] K. A. Benavidez,[1] G. A. Chandler,[1] S. W. Cordaro,[1] J. R. Fein,[1] E. S. Field,[1] S. B. Hansen,[1] P. F. Knapp,[1,b] J. Jackson,[1] R. J. Kaye,[1] M. Lowinske,[1] L. M. Lucero,[1] C. E. Myers,[1,c] M. A. Mangan,[1] O. M. Mannion,[1] B. Norris,[1] R. R. Paguio,[2] L. Perea,[1] A. J. Porwitzky,[1] P. K. Rambo,[1] G. K. Robertson,[1] D. C. Rovang,[1,d] F. Sanchez,[1] M. E. Savage,[1] M.-A. Schaeuble,[1] G. A. Shipley,[1,e] J. E. Shores,[1] G. E. Smith,[2] I. C. Smith,[1] C. S. Speas,[1] J. Taylor,[2] K. Tomlinson,[2] K. A. Whittemore,[1] J. M. Woolstrum,[1] E. P. Yu,[1] D. J. Ampleford,[1] K. Beckwith,[1,f] M. E. Cuneo,[1] E. C. Harding,[1] M. C. Jones,[1] R. D. McBride,[1,g] K. J. Peterson,[1] J. L. Porter,[1] G. A. Rochau,[1] J. Schwarz,[1] and D. B. Sinars[1]

AFFILIATIONS

[1]Sandia National Laboratories, Albuquerque, New Mexico 87185, USA
[2]General Atomics, San Diego, California 92121, USA

[a]**Author to whom correspondence should be addressed:** mrgomez@sandia.gov
[b]Presently at Pacific Fusion Corporation, Fremont, CA, USA
[c]Presently at Commonwealth Fusion Systems, Devens, MA, USA
[d]Presently retired
[e]Presently at Los Alamos National Laboratory, Los Alamos, NM, USA
[f]Presently at Lawrence Livermore National Laboratory, Livermore, CA, USA
[g]Presently at Nuclear Engineering and Radiological Sciences Department, University of Michigan, Ann Arbor, MI, USA

ABSTRACT

Magnetized liner inertial fusion (MagLIF) experiments have demonstrated fusion-relevant ion temperatures up to 3.1 keV and thermonuclear production of up to 1.1×10^{13} deuterium–deuterium neutrons. This performance was enabled through platform development that provided increases in applied magnetic field, coupled preheat energy, and drive current. Advanced coil designs with internal reinforcement enabled an increase from 10 to 20 T. An improved laser pulse shape, beam smoothing, and thinner laser entrance foils increased preheat energy coupling from less than 1 to 2.3 kJ. A redesign of the final transmission line and load region increased peak load current from 16 to 20 MA. The wider range of input parameters was leveraged to study target performance trends with preheat energy, applied magnetic field, and peak load current. Ion temperature and neutron yield generally followed trends in two-dimensional clean Lasnex calculations. Stagnation performance improved with peak load current when other input parameters were also increased such that convergence was maintained. This dataset suggests that reducing convergence to less than 30 would improve predictability of target performance. Lasnex was used to identify a simulation-optimized scaling path, which suggests 10+ kJ of fusion yield is possible on the Z facility with achievable input parameters. This path also indicates >10 MJ could be generated through volume burn on a future facility with a path to high yield (>200 MJ) using cryogenic dense fuel layers. The newly developed MagLIF platform enables exploration of both this simulation optimized scaling path and a recently developed similarity-scaling path.

I. INTRODUCTION

Production of significant thermonuclear fusion yield requires a confinement scheme to contain the extreme plasma temperatures (order of 10 keV). In the laboratory, two disparate confinement schemes have been developed: magnetic and inertial. In magnetic confinement fusion (MCF), a large volume (10^8 cm^3) of low-density

(10^{14}/cm^3) plasma is confined for long duration (>10 s) using large magnetic fields (10 T).[1,2] At the other extreme, in inertial confinement fusion (ICF), a small volume (10^{-7} cm^3) of high-density (10^{26}/cm^3) plasma is confined by the inertia of the fuel itself for short duration (10^{-10} s).[3–6] Magneto-inertial fusion (MIF) concepts utilize a combination of magnetic fields and inertial confinement to reach fusion conditions at intermediate densities and volumes for intermediate timescales.[7–10] Magnetized liner inertial fusion (MagLIF)[11] is a magneto-inertial fusion concept that sits much closer to the ICF limit than the MCF limit with typical values for volume, density, and duration of 10^{-4} cm^3, 10^{23}/cm^3, and 10^{-9} s.[12–14] MagLIF experiments have demonstrated thermonuclear neutron production[15–17] and sufficient magnetization at stagnation to trap charged fusion products,[18–20] which are key requirements for scaling a MIF concept to ignition.

In the MagLIF concept, the target consists of a hollow cylinder (called a liner) that contains fusion fuel (see Fig. 1). Most MagLIF experiments have used beryllium liners, and the fuel has been gaseous deuterium. An axial magnetic field (order of 10 T) is applied to the target using external field coils,[21] the fuel is heated to hundreds of eV by the multi-kJ Z-beamlet (ZBL) laser,[22,23] and the current from the Z machine[24,25] is driven axially through the target, causing it to magnetically implode. The Z machine delivers up to 1.4 MJ of electrical energy to the MagLIF load with a peak electrical power of up to 75 TW.[26] The applied magnetic field reduces radial thermal conduction throughout the implosion, which is critical to allow the preheat energy deposited by the laser to remain in the fuel to stagnation while the imploding liner does PdV work on the fuel, heating it quasi-adiabatically. The magnetic field is amplified through flux compression during the implosion, producing kT magnetic fields at stagnation, which are capable of trapping charged fusion products. Preheat is required to reach fusion conditions at achievable convergence ratios ($CR = R_{fuel,init}/R_{fuel,stag}$) due to the relatively slow implosion in MagLIF (<100 km/s), which provides negligible shock heating.[11] The slow implosion is well matched to the pulsed power generator (100 ns rise time) and allows relatively thick liner walls that are more robust to instability development.[27–32]

The MagLIF concept is critically dependent on successful magnetization, preheat, and target implosion to achieve fusion conditions. MagLIF experiments that include these three key components have produced burn-averaged ion temperatures up to 3.1 keV and primary deuterium–deuterium (DD) neutron yields up to 1.1×10^{13}.[17] These experiments produce significant x-ray emission from a high aspect ratio fuel column (height of column ≫ radius of column) at stagnation. Experiments conducted without either the preheat or the applied magnetic field generate on the order of 1×10^{10} neutrons and produce significantly less x-ray emission from the fuel column, as shown in Fig. 1.

Previous computational studies[11] have shown laser preheat is required to increase the fuel adiabat, which allows the liner implosion to do sufficient work on the fuel to reach fusion temperatures at an attainable CR. In z2744 (10 T, 0 kJ preheat, 16–17 MA), the x-ray

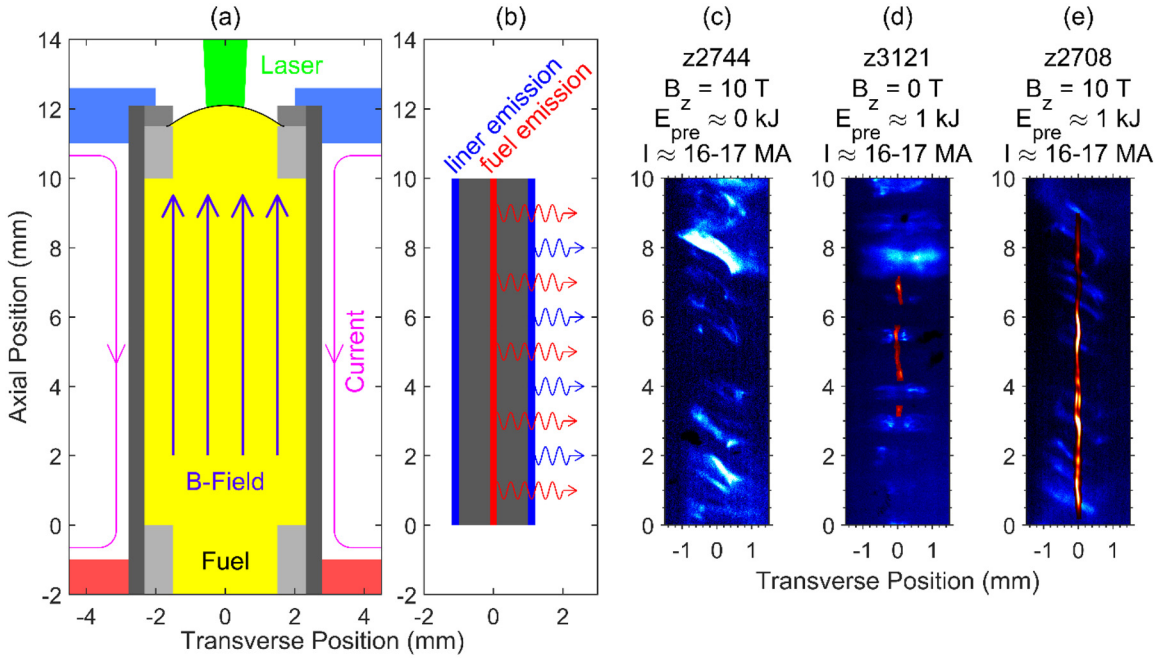

FIG. 1. (a) Diagram of the initial target geometry for MagLIF along with the three key components: applied magnetic field, laser preheat, and current-driven implosion. The deuterium fuel (yellow) is axially magnetized (purple arrows). The laser (green) enters the target axially, preheating the fuel to ~100 eV. The current (pink arrows) flows axially through the beryllium target (gray) generating a radially inward force that implodes the target. (b) Diagram depicting the approximate stagnation geometry. X-ray emission from the fuel on axis is significantly attenuated by the surrounding beryllium liner. Photons emitted by the fuel in the 5–15 keV range are observable. These are represented in the red color scale in (c)–(e). Photons from the beryllium liner are typically in the <5 keV range and are represented by the blue color scale in (c)–(e). The images shown in (c)–(e) were collected with a single spherically bent crystal imager[33] and processed, so emission from the fuel column is shown on the red color scale and emission from the exterior of the liner is shown on the blue color scale. X-ray self-emission images from (c) z2744 (10 T, 0 kJ preheat, 16–17 MA) (d) z3121 (0 T, ~1 kJ preheat, 16–17 MA), and (e) z2708 (10 T, ~1 kJ preheat, 16–17 MA) are shown.

image shows emission from helical structures on the exterior of the liner, but there is no observable emission from the fuel column [see Fig. 1(c)]. This experiment produced no measurable neutron peaks on the neutron time-of-flight (nTOF) detectors, and a DD neutron yield of 1×10^{10} was inferred from indium activation samples.

In simulations[34] of unmagnetized targets, the fuel reaches similar conditions during the preheat stage as in the magnetized case, though the spatial distribution of preheat energy varies. However, in the unmagnetized case, most of the energy is lost through thermal conduction to the cold liner walls during the implosion. In z3121 (0 T, 1 kJ preheat, 16–17 MA), the x-ray image shows weak emission from the fuel at only a few axial locations indicating an irregular stagnation column. Emission from the exterior of the liner in the absence of an axial magnetic field has azimuthally correlated features [see Fig. 1(d)]. The signal detected from the fuel is ~1/3× the signal from the exterior of the liner. A weak DD peak was recorded on the nTOF detector, and a DD yield of 4×10^{10} neutrons inferred from indium activation samples confirms poor neutron production in the absence of an applied axial magnetic field.

Demonstration of significant neutron production, as well as evidence of a hot fuel column, is observed when all three components of MagLIF are included. In z2708 (10 T, 1 kJ preheat, 16–17 MA), x-ray emission from the fuel was >10× brighter than x-ray emission from the helical structures on the exterior of the liner [see Fig. 1(e)]. Ion temperatures ranging from 1.1 to 3.1 keV and DD neutron yields ranging from 1.6×10^{11} to 1.1×10^{13} have been observed in MagLIF experiments with stagnation performance depending on the input parameters and mix levels in the experiment.[17] The significant increase in temperature and neutron production when all three key components of the MagLIF concept are included is consistent with predictions from simulations.[35]

Notably, MagLIF experiments have also been conducted on the Omega laser facility, where the target implosion is driven via ablative pressure on the exterior of the target as opposed to the magnetically driven implosions fielded on the Z facility.[36–38] These experiments were roughly 10% of the spatial scale, 1% of the temporal scale, and 0.1% of the energy scale of experiments on the Z facility. In the Omega experiments, target performance was enhanced when laser preheat and an applied magnetic field are included, similar to in Z experiments.[39,40] The successful demonstration of the MagLIF concept over a wide range of driver energies increases confidence in scaling predictions.

A key goal[41] of the United States ICF program[42] is to develop a laboratory platform that is capable of producing high fusion yield (>200 MJ). Recent results on the National Ignition Facility (NIF) have demonstrated multi-MJ yields are achievable in the laboratory.[43–45] Scaling calculations[35] in the two-dimensional magnetohydrodynamics (MHD) code Lasnex[46] indicate that MagLIF could produce multi-MJ fusion yields with peak load currents of 30–40 MA, and 10–100 MJ yields at 50–60 MA, as shown in Fig. 2. In these simulations, the target aspect ratio ($AR = R_{outer}/\Delta R_{wall}$) was fixed at 6, and the applied magnetic field was fixed at 30 T, while the target diameter, target length, initial fuel density, and coupled preheat energy were varied to find the optimum fusion yield for a given pulsed power circuit. At higher currents, the required preheat energies are comparable to the energy in one quad of the NIF. MagLIF preheat experiments have been conducted on the NIF and have demonstrated nearly 30 kJ of preheat energy coupled to the fuel.[47]

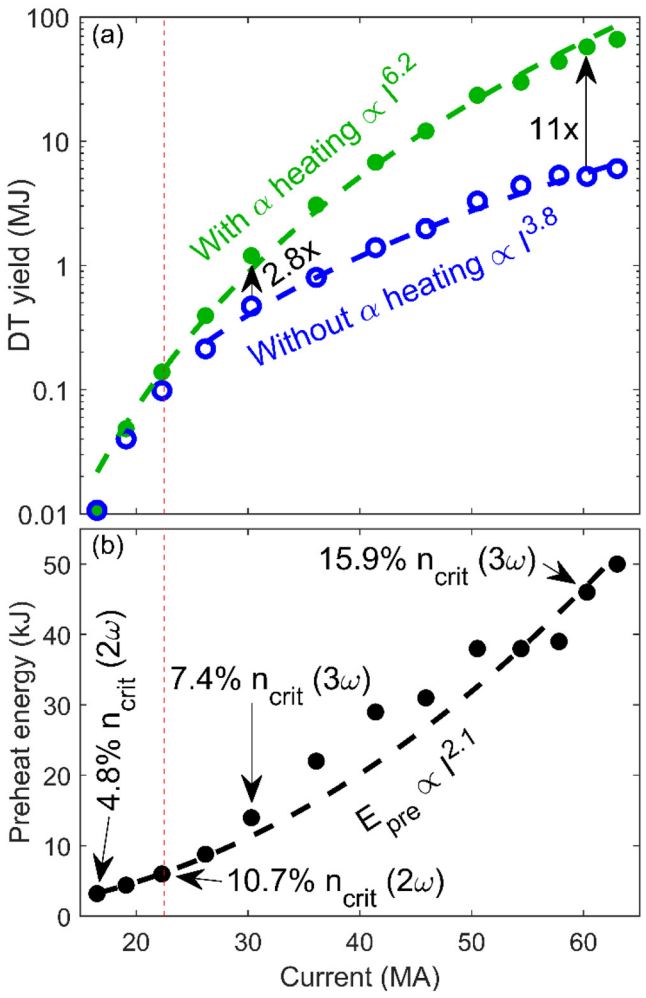

FIG. 2. (a) A plot of fusion yield as a function of peak load current from a series of 2D clean Lasnex calculations where the target aspect ratio (AR) and initial applied magnetic field were held fixed at 6 and 30 T, respectively, and the target diameter, initial fuel density, preheat energy coupled to the fuel, and target height were allowed to vary to find the optimal yield (green dots). The optimized configurations were rerun with alpha heating turned off (blue circles). Yield doubling occurred at roughly 30 MA, and yield increased by an order of magnitude at roughly 60 MA for these volume burn configurations. The vertical red dashed line indicates the approximate upper limit of achievable peak current for a MagLIF experiment on the present-day Z facility. (b) A plot of the required preheat energy in the optimized simulations with the fuel density represented for a few key simulations.

In Fig. 2, yield-doubling from alpha heating occurs around 30 MA, and at 60 MA, the yield increases by roughly an order of magnitude due to alpha heating. The impact of alpha heating increases gradually with increasing current (and coupled energy) as expected for volumetric ignition. These results are consistent with previous work[11,48,49] assessing MagLIF performance with driver energy beyond that of the Z facility. Similar calculations[50–52] indicate that yields greater than 100 MJ are possible at >55 MA in targets with DT-ice layers.[53] A similarity-scaling path[54–56] for MagLIF has also been

explored both analytically and computationally. The predicted performance along that path is comparable to the simulation-optimized scaling path, though the target dimensions and other input parameters at a given peak load current differ.

It is worth noting that two-dimensional "clean" calculations were used in generating the simulation-optimized scaling path. These 2D simulations cannot account for the impact that 3D structure has on performance. Moreover, the axial resolution of the simulations was chosen such that 2D instability growth was minimal since it is not representative of the 3D instability structures observed experimentally. The simulations also do not include a mix model (though an initial estimate of the impact of deceleration mix on target performance indicates a factor of 2–3 reduction in yield should be expected[35]). Additionally, laser preheat is not simulated, rather the preheat energy is deposited in an axially uniform column of the fuel. For these reasons, the simulations are expected to overestimate the performance in MagLIF targets; however, they indicate an interesting path exists for MagLIF and justify experimental scaling studies of the concept.

The highest achievable peak load current for MagLIF on the present-day Z facility is likely $\leq$22 MA, so the predictions of multi-MJ fusion yield around 30–40 MA cannot be directly tested without a larger pulsed power facility or a significant upgrade to the Z facility. In order to increase confidence in the extrapolation of MagLIF performance to multi-MJ yields, two key thrusts are being pursued: (1) demonstrate target performance scales as predicted by theory and in simulations over as wide a range of input parameters as is possible on the Z facility, and (2) evaluate target performance with input parameters as close as possible to those on the simulation-optimized scaling curve for the peak currents that are achievable on the Z facility. Both of these thrusts require increasing the input parameters beyond those available with the initial platform developed for MagLIF experiments.

This article focuses on the ongoing development of the MagLIF platform, which has enabled studies of target performance as a function of preheat energy, applied magnetic field, and peak current. The article is organized as follows: Sec. II describes the development of several new branches of the MagLIF platform that enable operation over a wider range of input parameters, Sec. III describes the results of experimental input parameter scans, and Sec. IV gives a summary.

II. DEVELOPING THE MAGLIF PLATFORM

Early MagLIF experiments were conducted with 10 T applied magnetic field, approximately 0.5 kJ of preheat laser energy coupled to the fuel, and up to 18 MA peak load current, producing up to 2×10^{12} DD neutrons (equivalent to 0.3 kJ of DT fusion yield).[14,15] According to two-dimensional clean Lasnex simulations, DT fusion yields in the 100 kJ range may be possible on the Z facility with increased input parameters (30 T, 6 kJ, 22.3 MA).[17,35] Subsections II A–II D describe the efforts to upgrade the MagLIF platform to enable increased applied magnetic field, preheat energy coupling, and load current, which required redesign of the final transmission line and applied magnetic field coil geometries, laser improvements, and target modifications.

A. Enhanced current coupling

Computational and analytic scaling studies for MagLIF span a range of currents from less than 15 MA to greater than 60 MA. Experiments on the Z facility will not be able to evaluate this full space, but they can be used to assess scaling predictions over a range of drive conditions at the lower end of this space. Experimental scaling studies are limited by diagnostic sensitivities, and Hydra[57,58] simulations suggest that roughly 12 MA is the minimum current at which stagnation would be diagnosable on the Z facility.[56,59] Most early MagLIF experiments were conducted at 16 MA,[14,60] providing a limited range for scaling studies. Development of the new MagLIF platform has enabled the Z facility to deliver increased current, expanding the range over which scaling can be studied.

The vacuum section of the Z facility includes four parallel outer transmission lines, a double post-hole convolute, a final transmission line, and a load volume (see Fig. 1 in Ref. 61). The outer transmission lines are driven in parallel to significantly reduce the overall inductance of the vacuum section, which is necessary to achieve the high current with short rise time of the Z facility. The convolute is a device that allows current carried by multiple parallel vacuum transmission lines to be combined into a single transmission line that delivers the current to the load. The outer transmission lines and convolute geometry generally remain fixed for all experiments on the Z facility, and the final transmission line and the load region are modified to meet the needs of each individual experiment.

To diagnose load current delivery, velocimetry measurements are made of the radial expansion of a magnetically driven thin-walled metallic cylinder, which is part of the return-current path in the load region. This geometry is modeled in an MHD simulation where the magnetic drive on the interior of the metallic cylinder is iteratively varied until the simulated velocity trace matches the experimental trace to within measurement uncertainty. This unfold is typically performed in 1D to limit computational expense, but 2D correction factors are applied when necessary.[62] The velocimetry measurement tightly constrains the peak load current delivered to the target, but the measurement is less sensitive to post-peak current, so it does not tightly constrain the current delivery at stagnation.[63]

In magnetically driven systems, the target is a part of the circuit, so it influences the current that the driver can deliver. The current that can be driven through a system is related to the inductance and voltage by

$$V = L\dot{I} + \dot{L}I, \tag{1}$$

where $V(t)$ is the driving voltage, $L(t)$ is the inductance of the system, and $I(t)$ is the current passing through the system. This means that the initial load inductance and target implosion trajectory (which sets $\dot{L}$) will feedback into the current that can be driven through the system. For a sense of scale, in MagLIF experiments on the Z facility the initial inductance within the vacuum section is up to 20 nH, the driving voltage at the vacuum insulating stack is roughly 4 MV, and the current is around 20 MA with approximately a 100 ns rise time. With a fixed driving voltage, higher inductance configurations result in a lower peak current and/or an extended rise time.

Current delivery in high power magnetically driven systems also is limited by current loss. The outer transmission lines on the Z facility were designed such that under normal conditions, they operate in an effectively lossless mode after magnetic insulation is established. Current losses in the convolute have been predicted in simulations[64–66] and observed experimentally.[67] Once losses in the convolute are initiated, there is a rapid impedance collapse to an essentially constant value[61,67] at which point losses are approximately proportional to the voltage at the convolute. Within the final transmission line, plasma formation on both the cathode and anode is expected.[68]

These plasmas reduce the effective anode–cathode gap, enhancing ion diode emission from the anode and increasing the possibility of current shunting through alternative paths rather than being delivered to the target. Thus, the design of the final transmission line and load region must limit the inductance to an acceptable level (~5 nH) to reduce losses within the convolute, and at the same time, the anode–cathode gaps must remain sufficiently large to minimize losses within the final transmission line itself.

In early MagLIF experiments, the final transmission line was designed around the geometry of the applied magnetic field coils. The footprint of the lower coil set both the minimum axial extent and the maximum radial position of the transmission line connecting the convolute to the load region. Three iterations of this general design with minimum anode–cathode gaps varying from 2 to 4 mm were evaluated in experiments on the Z facility prior to the first magnetized experiments [the 3 mm configuration is shown in Fig. 3(a)]. In the 2-mm configuration, asymmetric current delivery was inferred from the velocimetry measurements, suggesting the small anode–cathode gap in the final transmission line resulted in azimuthally varying losses. The 3- and 4-mm configurations had uniform current delivery, and the lower inductance, 3-mm configuration delivered a larger peak current. The inductance of the final transmission line [blue region in Fig. 3(a)] in the 3 mm configuration was 3.22 +/− 0.02 nH.[69]

The load volume is defined as the region between the target and the return current path (shown as red regions in Fig. 3), and in early MagLIF experiments, this volume was also highly inductive. Typically, the return current path consists of conductive posts separated by diagnostic apertures, which results in azimuthal variations in the magnetic field within the load volume. These azimuthal variations in the field are largest at the radial position of the return current path and decrease in amplitude near the target. In early MagLIF experiments, the return current path radius was set at 13 mm to minimize the potential for this azimuthal magnetic field asymmetry to imprint on the target implosion and drive flute modes. In some experiments, an azimuthally continuous beryllium annulus, which has a relatively low x-ray opacity enabling x-ray diagnostic access without apertures, was used to eliminate azimuthal variations in the magnetic field.

In early MagLIF experiments with a 10 mm tall imploding region, the axial extent of the load volume was 11.8 mm, and the target radius was 2.79 mm, resulting in an initial inductance of 3.66 ± 0.02 nH assuming an azimuthally continuous return current path. The diagnostic apertures in the return current path increased the magnetic volume slightly compared to a solid return current path, adding 0.34 ± 0.05 nH (values determined from Ansys Maxwell calculations) to the load volume resulting in a load inductance of 4.00 ± 0.05 nH. In z2851, the total inductance of the load volume and final transmission line was 7.22 ± 0.06 nH, and a peak load current of 15.8 ± 0.5 MA was inferred from velocimetry measurements.[14]

Circuit modeling[70] of z2851 indicates that in the absence of losses, the peak load current in this experiment could have been 21.8 MA. The significant discrepancy between the current from the lossless circuit model and the experimentally measured value indicates this configuration experiences multi-MA current losses. Notably, even in the absence of those losses, the high inductance of this configuration would significantly limit the achievable peak load current.

As implied above, modifications to the final transmission line and applied magnetic field coil designs are coupled. Constraints on the axial magnetic field uniformity and strength set requirements on the footprint of the lower magnetic field coil, which places limitations on the geometry of the final transmission line. Conservatively, the initial coil configuration for MagLIF was designed to maintain a variation of less than 1% in magnetic field across the target height; however, this constraint significantly limits transmission line design.

To understand the importance of axial uniformity of the magnetic field, a series of 2D MagLIF simulations were conducted in Lasnex with an axial gradient in the magnetic field of up to 50%. In these simulations the gradient in magnetic field was not critical, and target performance scaled with the average applied magnetic field in the target. Additionally, 3D simulations in Hydra show that during the laser preheat stage, the axial magnetic field is significantly redistributed leading to variation in magnetization even for an initially uniform applied magnetic field.[71] Based on this simulation guidance, the requirement on magnetic field uniformity was relaxed, allowing the lower magnetic field coil to be modified or even eliminated.

In the initial attempt to reduce the inductance of MagLIF experiments, the bottom coil was eliminated, which allowed for a significantly reduced axial extension of the final transmission line. Additionally, the axial extent of the load region was reduced to match

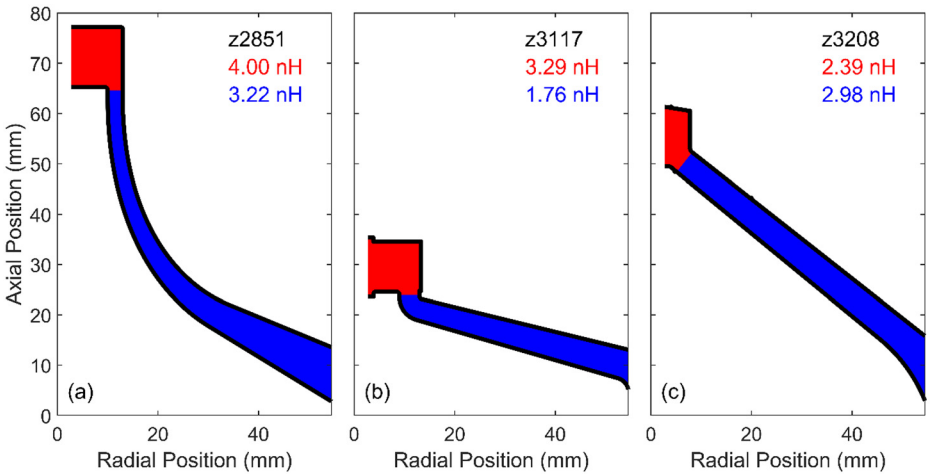

FIG. 3. Final transmission line and load geometries and the associated initial inductances from (a) z2851, (b) z3117, and (c) z3208. Black lines indicate the electrode surfaces. Red shaded regions indicate the load volume, and blue shaded regions indicate the final transmission line volume. Example shot numbers for each configuration are given in the upper right corner in black. Initial load inductances are listed in red and final transmission line inductances are listed in blue.

the imploding height of the target. This allowed the total inductance of the load region and final transmission line to be reduced to 5.05 ± 0.04 nH (z3117) while increasing the minimum anode–cathode gap in the final transmission line from 3 to 4 mm [see Fig. 3(b)]. This change resulted in an increase in peak load current from 15.8 ± 0.5 to 17.9 ± 0.3 MA (see Fig. 4). The lower inductance reduced the electrical stress in the convolute and improved current delivery to the load; however, this design primarily focused on removing inductance from the final transmission line. The inductance of the load volume remained relatively large, placing a high electrical stress at the end of the final transmission line, where the smallest anode–cathode gap exists.

The three parameters controlling the initial inductance of the load volume are target outer radius, target height, and return current path inner radius. The target outer radius and height cannot be changed freely as they impact the performance of the target, leaving the return current path radius as the only free design parameter to reduce the load volume inductance. As stated above, the return current path radius was typically set at 13 mm to limit the development of flute modes due to azimuthal asymmetries in the driving magnetic field, resulting in relatively large load volume inductances on all early MagLIF experiments. In z3208, the return current path radius was reduced to 7.79 mm creating a 5 mm radial anode–cathode gap between the target and the return current path and shrinking the load inductance by over 1 nH.

A new conical final transmission line was designed to connect to the smaller radius return current path [see Fig. 3(c)]. The transmission line tapers from a 6 mm anode–cathode gap near the convolute to a 5 mm anode–cathode gap at the entrance to the load volume. In this configuration, the inductance of the final transmission line is 2.98 ± 0.02 nH and the inductance of the load volume is 2.39 ± 0.03 nH, so the total inductance is 5.36 ± 0.05 nH. While this inductance is higher than in z3117, this new configuration delivered a peak current of 20.0 ± 0.2 MA to the load (z3208, z3209). This implies (1) significant losses occurred in the final transmission line on z3117, and (2) the new design tested in z3208 reduced those final transmission line losses. However, the circuit model indicates with the lower inductance of the conical configuration, the Z machine could deliver up to 23.7 MA to the load in the absence of losses, so there are still multi-MA losses in this configuration. Note that this conical design has not been optimized; increasing the peak load current to >20 MA is possible with further design iteration.[72,73]

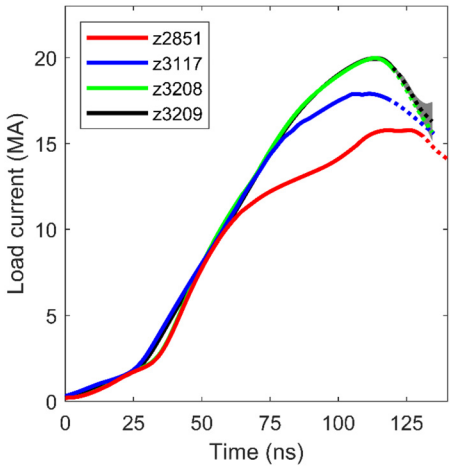

FIG. 4. Plot of load current traces for a series of 10 mm tall, 2.79 mm outer radius, AR6 targets inferred from velocimetry measurements. The dotted portions of the lines after peak current indicate increased uncertainty in the measurement. For z3209, the uncertainty in the measurement is indicated with a gray band.

A subtlety of the z3208 design is that the return current path transitions from conical to axial at approximately 1.9 mm above the bottom of the target. This geometry presents a fabrication challenge for beryllium parts, so the return current path must either (1) be manufactured from aluminum with diagnostic apertures to view the full target height and introduce seeds for flute modes, or (2) utilize azimuthally continuous beryllium cylinders to view the top 8.1 mm of the target and clip diagnostic access to the bottom 1.9 mm of the target. The former option has been used in all experiments with this transmission line and load configuration to date. ALEGRA[74] simulations of the target and return current path geometry conducted in 2D r-theta show that the number and position of diagnostic apertures can impact the symmetry of the implosion. Efforts to understand the impact of these asymmetries on target performance are discussed in Ref. 75.

B. Applied magnetic field coil development

The applied axial magnetic field in early MagLIF experiments was nominally 10 T. Previous simulation studies indicate that MagLIF performance on the Z facility would increase with increasing magnetic field up to around 30 T,[35] though at higher currents the optimal magnetic field decreases to around 15 T.[50] In the systematic-scaling framework,[56] the applied magnetic field scales as $I^{0.65}$ with ∼30 T required at 60 MA to conserve thermal conduction losses. Improvements to the applied magnetic field capability are of interest. Two main constraints limited the available applied magnetic field in early experiments: (1) maximum radial diagnostic access was required and (2) axial uniformity of the magnetic field was required to be better than 1%.[21]

With the above constraints, the load hardware geometry shown in Fig. 5(a) was used in early MagLIF experiments. This configuration allowed for radial diagnostic access as well as partially obstructed diagnostic access at 12° above radial, where many of the standard diagnostics[76–78] at the Z facility were positioned. Subsequent investment in the development of additional radial diagnostics[33,79–82] allowed for the reduced diagnostic access configuration shown in Fig. 5(b), which enabled nominally 15 T while maintaining 1% axial uniformity, but eliminated the 12° diagnostic line of sight.[21] Further increases in the applied magnetic field to 25 T with a uniform magnetic field are possible at the expense of eliminating radial diagnostic access,[21] though this would limit understanding of target performance, so it has not been pursued.

Relaxing the 1% uniformity constraint enables a path to higher fields while maintaining radial diagnostic access. The magnetic field coil configuration in Fig. 5(c) has enabled 20 T with 9% axial uniformity, where the uniformity is defined as

$$uniformity = \frac{2 * (B_{max} - B_{min})}{B_{max} + B_{min}} \quad (2)$$

with B_{max} and B_{min} representing the maximum and minimum axial magnetic fields within the target, respectively. In the configuration shown in Fig. 5(c), the coil above the target more strongly magnetizes

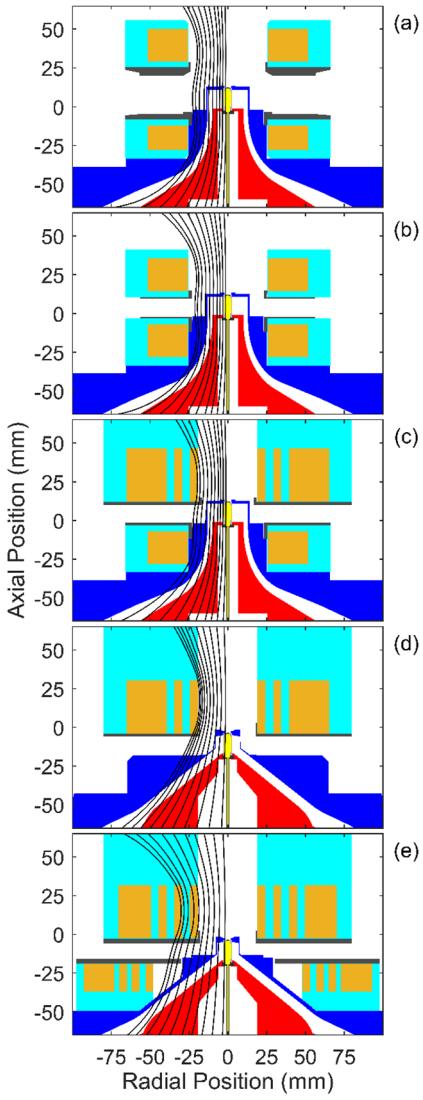

FIG. 5. Cross sections showing the applied magnetic field coil geometries for several MagLIF configurations. Cathodes are shown in red, anodes in blue, coil windings in orange, coil insulation and reinforcement in cyan, coil support hardware in the dark gray, beryllium target components in light gray, and fuel in yellow. Some example magnetic field lines are overlaid on the left half of the geometry in black. The nominal average magnetic field, field uniformity, and peak current for a 10-mm tall target for each configuration are (a) 10 T, <1%, 16–17 MA, (b) 15 T, <1%, 16–17 MA, (c) 20 T, 9%, 16–17 MA, (d) 15 T, 30%, 20 MA, and (e) 20 T, 17%, 20 MA. Lower fields can be achieved in each configuration. Magnetic field lines cross the anode–cathode gap in the final transmission line for all configurations, but this does not measurably impact the current delivery to the target.[87]

the target than the one below. Development of this stronger coil required a new capability to internally reinforce the windings within the coil due to the increased forces applied to the windings at higher magnetic fields.[83] Several configurations of this internally reinforced coil have been developed including versions with 3, 4, and 5 sets of windings, called sub-coils. Figure 5(c) shows a version with three sub-coils, and Fig. 5(e) shows a version with four sub-coils. The number of sub-coils has a small impact on the achievable field and uniformity. Notionally, the bottom coil in Fig. 5(c) could also utilize internal reinforcement to enable higher magnetic fields with improved axial uniformity in the target; however, this configuration is not optimized for current delivery to the target, so the development of such a coil has not been prioritized.

Utilizing the internally reinforced coil described above and the conical transmission line shown in Fig. 3(c), an AR6 target with a 10-mm tall imploding region can be magnetized to nominally 15 T average magnetic field by the fringe field of the coil with 17.2 T at the top of the target and 12.8 T at the bottom (axial uniformity = 30%) while simultaneously allowing a peak current of up to 20 MA. The single coil sits just above the target, allowing radial diagnostic access to the target. This configuration [shown in Fig. 5(d)] has become the standard load hardware configuration for MagLIF experiments. The vertical extension of the conical section was included to provide space for an advanced lower coil as shown in Fig. 5(e). This configuration has demonstrated >20 T average magnetic field with 17% uniformity in offline tests, but it has not yet been incorporated in experiments on the Z facility. The different radial extent of the coils in Fig. 5(e) creates a torque on the support structure separating the coils, which has proven challenging to robustly support. Further updates to this dual advanced coil design are under way[83] with the goal of simultaneously magnetizing the target to an average of 20 T and driving the target with 20-MA peak current on the Z facility.

Note that alternative methods for generating axial magnetic fields within the target without using external coils are also under development. Targets with helical conducting paths[84] have demonstrated axial fields as high as 200 T on the Z facility.[85] Similarly, helical return current paths can introduce ~10 T axial magnetic fields within the target.[86] These technologies have not yet been utilized in MagLIF stagnation experiments and are not discussed further in this work.

C. Laser preheat improvements

Early MagLIF experiments were conducted with roughly 0.5 kJ of laser energy deposited in the fuel. For the peak load currents accessible on the Z facility, the simulation-optimized curve in Fig. 2 assumes preheat energies between 3.2 and 6 kJ. To approach this optimized performance, significant improvements to the laser coupling are required. The main limitations on preheat energy coupling are as follows: (1) the laser energy delivered to the target, (2) the loss of energy to absorption in the laser entrance window material, (3) the loss of energy due to backscatter, and (4) any laser energy penetrating beyond the target implosion region.

The laser pulse shape has been significantly modified to increase the total laser energy delivered to the target. The original laser preheat pulse shape for MagLIF is shown in Fig. 6 (z3135). It contained a total of ~2.5 kJ between the pre-pulse and main pulse at the output of the laser, but losses in the optics chain result in closer to 2 kJ on target.[14] The available energy in the laser was increased to roughly 4 kJ by adding additional amplifiers and replacing the frequency doubling crystal to improve conversion efficiency and enable longer pulses. To take advantage of the greater available energy, the bandwidth of the laser was increased, reducing the risk of stimulated Brillouin scattering within the optics.[88] Taking into account for the efficiency of the optics chain, this enables up to 3.4 kJ on target under ideal conditions.

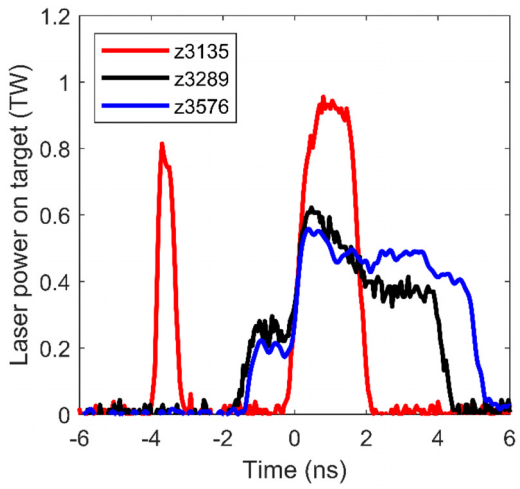

FIG. 6. Plot of the laser power on target for the original MagLIF laser configuration (red), the configuration used in more recent room temperature experiments (black), and the configuration used in recent cryogenically cooled experiments (blue). Coupling efficiency increased from 25% to 50% with the red pulse shape to 89% with the blue pulse shape.

The energy lost to absorption in the LEH window foil is roughly proportional to the foil mass with which the laser beam interacts. This mass increases as lR_{beam}^2, where l is the foil thickness and R_{beam} is the radius of the laser spot; thus, a small spot and a thin window minimize absorption losses. However, at high intensity, laser-plasma instabilities due to the laser interaction with the LEH foil and the fuel can cause a significant fraction of the laser energy to be lost through backscatter.[89,90] This motivated an effort to reduce laser intensity through beam smoothing and increased spot size.

The unconditioned ZBL laser spot has significant nonuniformities with high-intensity regions. Introducing a distributed phase plate (DPP) optic that generated a 1.1-mm-diameter beam size smoothed the intensity variations in the beam profile and lowered the intensity by increasing the laser spot size from approximately 0.25 to 0.95 mm^2. In combination with the lower power laser pulse, the intensity on target was decreased from $\sim 4 \times 10^{14}$ to $\sim 5 \times 10^{13}$ W/cm^2. With the 1.1-mm DPP optic, the energy lost to stimulated Brillouin backscatter decreased from ~0.5 to ~0.02 kJ.[90] Increasing the area of the laser spot size also helps control the deposition length. However, the increase in laser-spot size resulted in an increase in the fraction of laser energy absorbed in the LEH window foil, so additional effort was focused on reducing the window thickness.

The LEH window foil is necessary to contain the deuterium gas within the target, and the minimum thickness of the foil is approximately linearly dependent on both the pressure of the gas and the diameter of the LEH. The minimum foil thickness, T_{LEH}, in μm is reasonably approximated by

$$T_{LEH} = 1.3\frac{D_{LEH}}{2.2}\frac{P_{fuel}}{8.27} + 0.3, \tag{3}$$

where D_{LEH} is the diameter of the LEH in mm and P_{fuel} is the pressure of the fuel in bar. Ideally, the diameter of the opening is at least twice the diameter of the laser spot size to minimize the interaction between the wings of the laser spot and the edges of the LEH. In the first MagLIF experiments, the LEH window foil was conservatively chosen to be 3.5 μm ± 10% (thickness prior to being deformed into a bubble) to contain 4.14 bar (60 psi) of deuterium at room temperature (fuel density = 0.68 mg/cm^3) with a 3-mm-diameter LEH. In this configuration, ~1 kJ of the energy incident on the target was lost due to interaction with the LEH window.[14] To reduce these losses, in subsequent experiments the foil thickness was reduced to 1.77 μm ± 10% for 3-mm-diameter foils containing 4.14 bar, enabling >1 kJ to be deposited in the fuel. The window was further reduced to 1.56 μm ± 10% for 2.2-mm-diameter foils containing 6.21 bar (90 psi), which enabled up to 1.4 kJ of preheat energy to be deposited in 1.03 mg/cm^3 fuel with the updated, lower power laser pulse shape shown in black in Fig. 6 (z3289). The increase in coupling efficiency from approximately 25% to over 50% is a significant improvement; however, additional increases in efficiency and laser energy on target are clearly required to reach the preheat levels in the optimized Lasnex simulations.

Further efforts to increase the preheat energy coupled to the fuel involve cryogenically cooling the target to reduce the fuel pressure while maintaining the fuel density. At 70 K, the fuel pressure required to reach a fuel density of 1.03 mg/cm^3 is roughly 1.52 bar (22 psi), which allows the LEH window thickness to be reduced to ~0.6 μm. With less window material, a larger spot size can be used without losing too much energy to absorption in the window. Alternative methods to eliminate the impact of the laser window on preheat energy have also been developed. A small electrical pulse[91] or a low energy laser[92] can be used to burst the window just prior to laser preheat. These technologies have not yet been utilized in MagLIF stagnation experiments and are not discussed further in this work.

Using a 1.5-mm-diameter laser spot and the low power, higher energy pulse shape shown in blue in Fig. 6 (z3576), 89% coupling was demonstrated with 2.3 kJ of preheat energy deposited in the fuel for 2.6 kJ on target.[93] With ideal transmission through the optics chain, up to 3.4 kJ could reach the target, allowing 3 kJ to be deposited in the fuel.

Increasing preheat further would require additional upgrades to the ZBL laser, which are possible but costly and time-consuming. The laser infrastructure notionally allows up to 6 kJ operation (though with the potential for significant optics damage), which could put up to 5.1 kJ on target and at 89% coupling, 4.5 kJ in the fuel. For comparison, 3D Hydra calculations suggest that 4.25 kJ could be deposited in the fuel with 5.5 kJ on target,[94] so 4.5 kJ deposited may be optimistic.

As the energy on target increases, the possibility of preheat energy penetrating beyond the target length becomes significant. The propagation depth of a laser pulse absorbed through inverse bremsstrahlung absorption can be approximated by[94]

$$z \simeq \frac{3.57N^{\frac{4}{5}}E_{preheat}^{\frac{3}{5}}}{\rho_{DD}^{\frac{7}{5}}R_{beam}^{\frac{6}{5}}}, \tag{4}$$

where z is the propagation depth in mm, N is the harmonic of a 1.054 μm laser, $E_{preheat}$ is the laser energy absorbed in the fuel in kJ, ρ_{DD} is the fuel density in mg/cm^3, and R_{beam} is the radius of the laser spot in mm. Based on this equation, to maintain the same propagation depth while increasing the energy deposited from 2.3 to 4.5 kJ, R_{beam} would need to increase from 0.75 mm to approximately 1.05 mm for a fuel density of 1.03 mg/cm^3. Conversely, the propagation depth could

be maintained with the available 1.5-mm DPP optic if the fuel density were increased to 1.4 mg/cm^3.

D. Target modifications

The targets in early MagLIF experiments had a 7.5-mm imploding height, as shown in Fig. 7(a). These targets also utilized aluminum and plastic fuel-facing components called "cushions" to mitigate the wall instability.[30,31] In subsequent experiments, the target was modified to (1) reduce radiative losses from mix, (2) reduce the fraction of fuel lost through the open ends of the cylindrical target, and (3) improve implosion stability.

As was discussed in Sec. II C, early MagLIF experiments had relatively low preheat energy coupling. As preheat energy was increased in subsequent experiments, increased mix from mid-Z fuel-facing components drove the plasma temperature and yield down relative to the initial experiments.[14,16] Improvements in target design and fabrication capabilities allowed the aluminum and plastic components to be replaced with beryllium. In the higher preheat limit, when all fuel-facing components were replaced with beryllium, the primary neutron yield increased by over an order of magnitude.[13] Following this observation, all fuel facing components have been made from beryllium to minimize the impact of laser-induced mix.

As the preheat energy increases, the mass of preheated fuel lost through the open ends of the target is also expected to increase, which can result in a higher target convergence at stagnation. This can be partially mitigated by increasing the target length to reduce the fraction of fuel mass lost. An additional benefit of a longer imploding region is localized mix from the LEH window material or cushions will occupy a smaller fraction of the axial extent of the fuel. However, longer targets require a proportional increase in preheat energy to reach the same average fuel temperature. Also, with everything else held constant, an increase in target length raises the load inductance, which results in a decrease in load current. Lasnex simulations, which did not account for mix, indicated similar target performance at 7.5 and 10 mm imploding heights. The target imploding height was increased to 10 mm for the majority of MagLIF experiments with the goal of minimizing the impact of axially localized sources of mix.

Additional modifications to the target have primarily focused on improving stability. It is worth noting that as the peak load current has increased (see Sec. II A), in general, the target inner and outer diameters have remained at 4.65 and 5.58 mm, respectively. The increase in magnetic pressure, combined with an unchanged target, results in a more aggressive implosion, which appears to be less stable (see Sec. III C). Several methods have been suggested to improve target stability including decrease the target aspect ratio (AR) to reduce instability feedthrough,[95] introduce a dielectric coating[95–98] to the exterior of the liner to reduce the impact of the electrothermal instability,[99–102] which acts as a seed for the magneto-Rayleigh–Taylor instability, and introduce a dynamically changing magnetic field to drive the target.[86,103–105] Based on the available datasets, the parameter scans in Sec. III include the standard AR6 target shown in Fig. 7(c) and the dielectric coated AR9 target shown in Fig. 7(d).

III. EXPERIMENTAL SCALING TRENDS

With the present MagLIF experimental platform, it is possible to deliver nominally 15 T applied axial magnetic field, 2.3 kJ of preheat to the fuel, and 20 MA peak load current simultaneously to an AR6, 10-mm tall target containing 1.03-mg/cc deuterium fuel. This enhanced platform has enabled studies of stagnation performance as a function of each of the input parameters in MagLIF. As described below, the experimental trends observed in these parameter scans were generally consistent with expectations from 2D clean Lasnex simulations. Additionally, experimental performance increased significantly when all input parameters were simultaneously increased, as expected.

Neutron yields discussed below were derived from indium activation samples and represent the primary deuterium–deuterium fusion neutrons. Ion temperatures were determined using a forward fit in

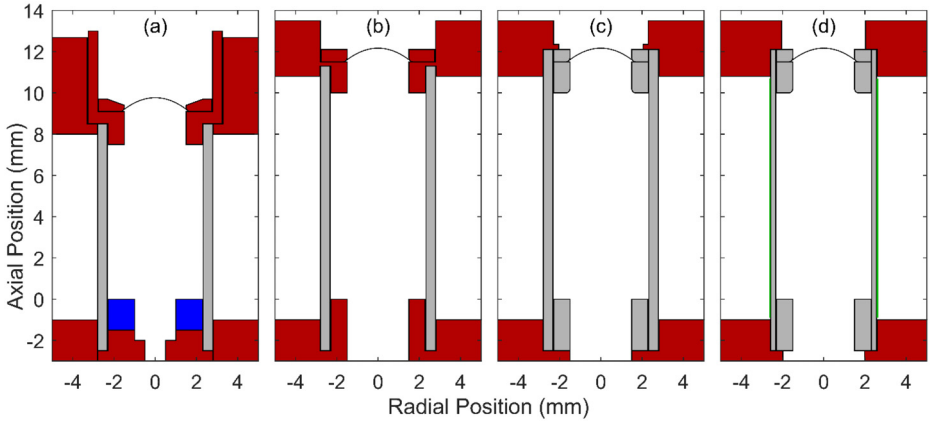

FIG. 7. Cross-sections of target geometries used in MagLIF experiments. Gray represents beryllium components, red represents aluminum components, blue represents nylon components, and green represents an epoxy coating. (a) This configuration had a 7.5-mm imploding region and was used primarily in 2013–2014. (b) This configuration increased the imploding region to 10 mm and was used primarily in 2014–2015. (c) In this configuration, the aluminum fuel facing components were replaced with beryllium. It has been used commonly since 2015. (d) This configuration incorporated a 75-μm-thick dielectric coating (Epon epoxy) on the exterior of the liner to stabilize the implosion. The mass/length of the beryllium and epoxy in this configuration matches an aspect ratio (AR) 9 beryllium liner. To compensate for the mass of the epoxy, the AR of the beryllium was increased to 10.6. This configuration was initially tested in 2016 and commonly used since 2017.

TABLE I. The input parameters, stagnation performance, and simulation values for the experiments described in this manuscript. Targets with an outer radius to wall thickness of 6 are listed as AR6. Targets with a dielectric coating and a mass/length equivalent to an aspect ratio 9 target are listed as cAR9. Initial fuel density values with * had significant uncertainty due to a large temperature gradient across the target. Preheat energy values with * had a misalignment of the preheat laser, which may have impacted energy coupling. Peak current values with * were not measured on the experiment, and a peak load current was assumed based on the measured peak current in experiments with identical transmission line and load geometries.

Shot	Target	Cryo	$\rho_{0,\text{fuel}}$ (mg/cc)	Applied B_z (T)	Preheat (kJ)	I_{peak} (MA)	Exp. yield	T_{ion} (keV)	Sim. yield	Sim. fuel CR
z2839	AR6	N	0.68	10.2	1.07	16*	3.2×10^{12}	2.2	5.9×10^{12}	39
z2977	AR6	N	0.68	9.6	0.87	16*	3.0×10^{12}	2.6	5.5×10^{12}	40
z3019	cAR9	N	0.68	9.7	0.93	15*	3.0×10^{12}	2.5	2.7×10^{13}	46
z3040	AR6	N	0.68	9.6	0.78	16*	4.1×10^{12}	2.6	5.2×10^{12}	40
z3075	cAR9	N	0.68	9.7	0.94	15.2	2.6×10^{12}	2.3	2.7×10^{13}	46
z3135	cAR9	N	0.68	9.8	1.00	15*	3.1×10^{12}	2.6	2.8×10^{13}	47
z3179	cAR9	N	0.68	15.8	0.95	15*	5.3×10^{12}	3.1	4.7×10^{13}	46
z3208	AR6	N	0.68	12.0	0.92	20.0	3.5×10^{12}	2.6	4.0×10^{13}	49
z3209	AR6	N	0.68	11.9	0.94	20.0	3.7×10^{12}	2.6	4.0×10^{13}	49
z3239	cAR9	N	0.68	20.0	0.9*	15*	2.0×10^{12}	2.6	...	...
z3240	cAR9	N	0.68	15.5	0.9*	15*	1.4×10^{12}	2.3	...	...
z3289	AR6	N	1.03	15.9	1.15	20*	1.1×10^{13}	3.1	5.2×10^{13}	41
z3292	AR6	N	1.03	16.1	1.36	20*	5.2×10^{12}	2.4	6.0×10^{13}	41
z3500	AR6	Y	1.03*	14.8	1.18	20*	3.0×10^{12}	2.3	...	...
z3501	AR6	Y	1.03*	14.7	1.26	19.8	3.1×10^{12}	2.2	...	...
z3576	AR6	Y	1.03	14.7	2.31	20.3	7.6×10^{12}	2.7	7.8×10^{13}	38

time–space to the deuterium–deuterium fusion neutron time of flight[106] measurement. The preheat energy coupled to the fuel was determined as described in Ref. 107. The applied magnetic field is determined based on the capacitor bank current and an appropriate scale factor for the coil geometry. Convergence ratio is determined using the average radius observed in x-ray self-emission imaging.[14,33] The peak load current was measured using velocimetry.[62] In experiments where velocimetry data are not available, the peak current was estimated based on comparison to other experiments with similar initial inductance and target geometry. Input parameters and stagnation conditions for the experiments discussed are listed in Table I.

A. Impact of preheat energy coupling

Early MagLIF experiments [using the target in Fig. 7(a)] demonstrated interesting stagnation conditions with less than 1 kJ of preheat energy coupled to the fuel. In subsequent experiments that used the target in Fig. 7(c), the neutron yield and ion temperature increased in the low preheat energy range and reached a performance plateau with higher preheat energy coupled to the fuel (see Fig. 3 in Ref. 17). The experimental trends in neutron yield, ion temperature, and fuel magnetization were all consistent with the trends predicted in clean two-dimensional Lasnex simulations. The enhanced preheat platform described in Sec. II C has expanded the range of preheat energies over which target performance can be studied.

A series of experiments (z3289, z3292) were conducted at an initial fuel density of 1.03 mg/cm^3 with 16 T applied magnetic field and 20 MA peak load current. In these experiments, the 1.1 mm spot size DPP was used, and the preheat energy was 1.15 and 1.35 kJ, respectively. Based on 2D clean Lasnex simulations, target performance begins to plateau in this range of preheat energy. Neutron yield and ion temperature decreased for the higher preheat energy experiment (see Fig. 8).

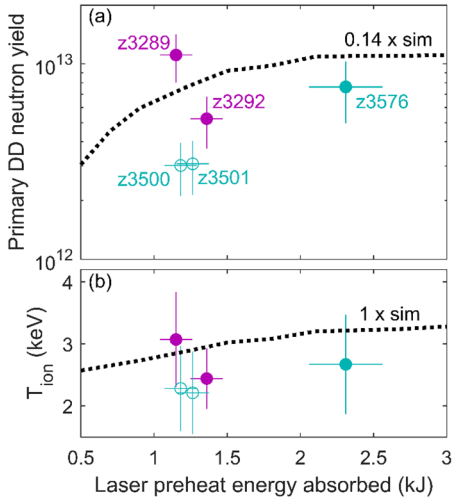

FIG. 8. Plots of the (a) primary DD neutron yield and (b) ion temperature as a function of preheat energy with experiments shown as circles and scaled 2D clean Lasnex simulation results shown as dotted lines. Experiments shown in magenta were conducted at room temperature, and experiments shown in teal were cryogenically cooled to approximately 70–120 K to enable compatible fuel densities at lower pressures. Experiments shown as open circles have caveats associated with their configuration, which may have impacted stagnation performance relative to the predictions from Lasnex simulations.

In 3D HYDRA simulations[94] of these experiments, ~1.15 kJ was close to the maximum energy that could be deposited in the fuel by the laser before reaching the bottom of the target. The ~0.2 kJ increase in preheat energy in z3292 may have been largely deposited into the bottom of the target, increasing mix and reducing stagnation performance. While additional laser-induced mix may have impacted performance in z3292, these experiments are among the highest performing, near repeat MagLIF experiments to date, so they were used as a reference point for additional studies.

Efforts to extend the range of available preheat energy rely on cryogenic target configurations. An attempt was made to replicate z3289/z3292 as closely as possible but with the addition of cryogenic cooling to demonstrate that the initial temperature of the target had a negligible impact on stagnation performance. The cryogenically cooled experiments (z3500, z3501) underperformed compared to their room-temperature counterparts, with neutron yields 41%–73% lower and ion temperatures 7%–28% lower. The cryogenic cooling does not appear to impact current coupling,[93] and previous efforts indicated ice growth on the LEH window should be negligible compared to the foil thickness;[108] however, a significant initial temperature gradient was noted across the target in both z3500 and z3501. This increased the uncertainty in the density of the fuel to roughly 25%. LASNEX simulations predict that MagLIF performance can be a strong function of preheat energy and initial fuel density, possibly explaining the observed difference.

An additional cryogenically cooled experiment (z3576) was conducted to explore the impact of further increasing preheat energy. In this experiment, cryostats were fielded on both ends of the target, resulting in a negligible temperature gradient across the target.[93] Additionally, the 1.5 mm spot size DPP was used to decrease laser intensity (reduced LPI concerns) and decrease the penetration depth of the preheat (reduced mix concerns). With these modifications, the preheat energy coupled to the fuel was increased to 2.3 kJ. This experiment produced 7.6×10^{12} DD neutrons with an ion temperature of 2.7 keV, which are comparable values to those of z3289 and z3292, as expected given the predicted plateau in performance over this preheat energy range.

Interestingly, in the cryogenic experiments, there is a significant change in the axial uniformity of the x-ray images compared to the room temperature targets. In room temperature targets, the brightest emission regions are on average $530 \pm 120\%$ brighter than the mean emission intensity, whereas in the cryogenic experiments, the brightest emission regions are only $200 \pm 10\%$ times brighter than the mean emission intensity. X-ray self-emission images and the axial emission intensity from z3289 and z3501 are shown in Fig. 9. The relative uniformity of x-ray images from the cryogenically cooled experiments is consistent with more uniform fuel conditions within the stagnation column. It may also indicate a change in MRTI structure, which could be caused by a change in the low-density plasma environment[109] due to vaporization of ice formed on the exterior of the liner in cryogenically cooled targets. More uniform conditions in the stagnation column and/or liner implosion are advantageous since they may result in improved reproducibility and higher confidence in scaling to higher currents and higher yields on a future facility. The impact of cryogenically cooled targets on stability will be the topic of a future study. Notably, university-scale pulsed power drivers may be well-suited to study changes in the low-density plasma environment for cryogenically cooled targets.

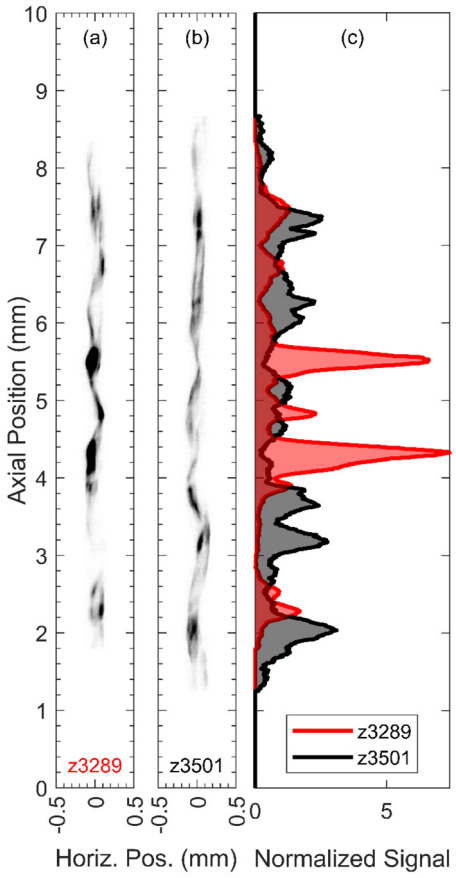

FIG. 9. (a) X-ray self-emission image from z3289. In the image, dark represents more intense emission. (b) X-ray self-emission image from z3501. (c) Plot showing the signal intensity normalized to the axially averaged emission intensity for z3289 (red) and z3501 (black).

B. Impact of applied magnetic field

In early MagLIF experiments, an applied magnetic field of 10 T was provided by the magnetic field coils shown in Fig. 5(a) as this configuration provided the greatest diagnostic access. Computational studies[35] indicated target performance would increase with stronger applied magnetic fields. Experiments were conducted using the target in Fig. 7(d) to evaluate stagnation performance as a function of the applied magnetic field, while all other parameters were nominally held constant. The initial fuel density for these experiments was 0.68 mg/cm^3 and the preheat energy was approximately 1 kJ. Note that despite using nominally the same transmission line and load region, due to the lower mass of the coated AR9 target, this configuration implodes sooner and reaches a lower peak load current of approximately 15 MA as compared to the AR6 target.[110]

A series of three experiments were conducted using this configuration at approximately 10 T, producing an average ion temperature of 2.4 ± 0.2 keV and on average $2.9 \times 10^{12} \pm 0.3 \times 10^{12}$ DD neutrons.[95] Increasing the applied magnetic field to 15.8 T using the coils shown in Fig. 5(b) resulted in 29% higher temperature and 83% higher neutron yield, as shown in red in Fig. 10. Two-dimensional clean LASNEX

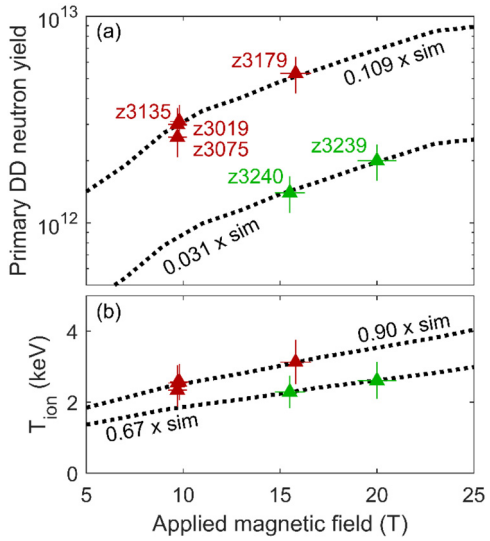

FIG. 10. Plot of the (a) primary neutron yield and (b) burn-averaged ion temperature as a function of the applied magnetic field for experiments (shown as triangles) and 2D clean LASNEX simulations (shown as dotted lines). The preheat configuration was intended to be identical across the experiments, but an alignment issue with the preheat laser may have resulted in reduced preheat energy coupling and/or enhanced laser induced mix in z3239 and z3240 (shown in green).

simulations of this configuration exhibit similar trends as those observed experimentally, though the simulations overpredict the ion temperature by a factor of 1.1 and the primary neutron yield by a factor of 9.2. Note that these simulations assumed a beryllium AR9 liner and ignored the dielectric coating used in the experiments for simplicity.

Two additional experiments (z3239 and z3240) were conducted to extend the range of the applied magnetic field scan (shown in green in Fig. 10) using the coils shown in Fig. 5(c). These experiments used the coated AR9 target with nominally the same initial fuel density, preheat energy, and peak load current as the previous magnetic field scan experiments (shown in red in Fig. 10). Notably, there is a significant discrepancy between stagnation performance across these two sets of experiments. The applied magnetic field in z3239 and z3240 did have a 9% axial gradient; however, as discussed in Sec. II A, this is not believed to be the source of the observed discrepancy. The preheat configuration for these experiments was intended to be identical to that used in the previous applied magnetic field scan, but a pointing error in the alignment of the laser beam was identified after the experiments were completed. This error may have resulted in decreased preheat energy coupling to the fuel and/or increased laser induced mix. Within this very limited dataset of two points, the experiments still follow the trends observed in simulations with ion temperature increasing by 14% and primary neutron yield increasing by 43% when the applied magnetic field increased from 15 to 20 T.

C. Impact of peak load current

Early MagLIF experiments utilized a high inductance final transmission line [see Fig. 3(a)] to deliver current to the load, which resulted in peak load currents in the 16 MA range for AR6 targets with 10-mm tall imploding regions. A lower inductance conical transmission line with larger anode-cathode gap spacing [see Fig. 3(c)] delivers 20 MA to that same target. A series of experiments (z3208, z3209) utilized this new conical transmission line to deliver a higher current while retaining roughly the same initial fuel density (0.68 mg/cm^3) and coupled preheat energy (0.9 kJ) with a marginal increase in average applied magnetic field (12 T). The two higher current experiments produced neutron yields of 3.5×10^{12} and 3.7×10^{12} and ion temperatures of 2.6 keV, which were comparable to the best performing experiments at lower currents. z3208 and z3209 are an example of reproducible target performance in MagLIF experiments conducted with nominally the same input conditions.

According to 2D clean LASNEX simulations, the increase in current from 16 to 20 MA was expected to produce a factor of 10× higher neutron yield, but the experiments essentially showed no change (see Fig. 11). These simulations also suggested that the convergence ratio would increase from 40 to 49 due to the increase in current. It is challenging to assess the experimental convergence in MagLIF. There are significant variations in the width of emission along the axial dimension of the target, suggesting that the convergence varies over the height of the column. Additionally, there is transverse structure in the images indicating a non-circular cross section of the stagnation column. With that said, an axially averaged convergence ratio was determined as described in Ref. 14. While there are systematic errors in this analysis, the same methodology was applied uniformly across the dataset allowing an assessment of the relative convergence of the experiments. The observed average convergence did increase slightly from 36 (at 16 MA) to 39 (at 20 MA); however, the uncertainty in the inference is significantly greater than the observed difference in the average convergence values. The available experimental data do not support the increase in convergence observed in the 2D clean LASNEX simulations, where target convergence was not limited by instabilities. Previous

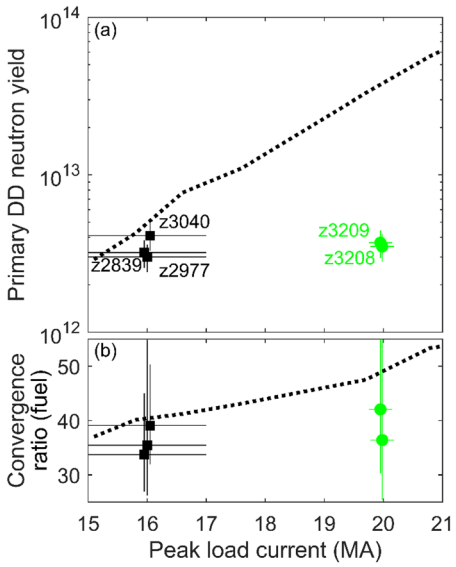

FIG. 11. Plots of the (a) primary neutron yield and (b) fuel convergence ratio as a function of peak load current for experiments (shown as squares and circles) and 2D clean LASNEX simulations (shown as dotted lines).

studies[111,112] with other ICF concepts have shown that instabilities limit the achievable convergence, and a comparison of the x-ray self-emission images in low and high current MagLIF experiments[17] appears to indicate a similar limit to convergence.

Lasnex simulations[35] suggest that increasing the initial fuel density, applied magnetic field, and preheat energy along with the current will result in increased yield without increasing convergence.[17] The experiments described in Sec. III A (z3289, z3292) had increased initial fuel density (1.03 mg/cm^3), applied magnetic field (16 T), and coupled preheat energy (1.15–1.35 kJ) relative to z3208 and z3209. Comparing the stagnation performance of z3289 and z3292 to z3208 and z3209, the average neutron yield more than doubled from 3.6×10^{12} to 8.2×10^{12}, and a decrease in the average inferred convergence ratio (39 to 31) was observed. The experimental-to-simulated yield ratio or "yield over clean" (YOC) also was improved for z3289 and z3292 relative to z3208 and z3209.

To better understand the relationship that stability has on experimental target performance, the YOC was plotted as a function of the predicted convergence ratio in Fig. 12 for the experiments discussed above excluding those with abnormal preheat and high uncertainty in initial fuel density. This plot shows 2D clean Lasnex simulations significantly overpredict yields for configurations with simulated fuel convergences >45. For configurations with lower simulated convergence, the discrepancy between simulation and experiment generally decreases. Similar behavior is observed in other fusion concepts: high convergence is favorable in simulations that neglect the impacts of implosion instabilities, but experiments do not match these simulations.[111,112] A curve parametrized as

$$YOC = 1 - \left(1 + e^{-\alpha(CR_s - \beta)}\right)^{-1} \quad (5)$$

can fit the data. Here, YOC is the ratio of the experimental yield the simulated yield for a configuration, and CR_s is the simulated convergence ratio for that configuration. According to this equation, in the limit where $CR_s \gg \beta$, YOC becomes small, and for $CR_s \ll \beta$, YOC approaches 1. Intuitively, these are the behaviors expected in these limits for fusion targets. The best fit to the data gives $\alpha = 0.191 \pm 0.048$ and $\beta = 36.7 \pm 2.5$ and is shown in cyan in Fig. 12. The reported confidence intervals for the fitted parameters are derived from a series of 1000 fits to a Monte Carlo sampling of the uncertainty distributions of the datapoints and represent a range of 2-σ. Figure 12 appears to indicate stagnation performance becomes more predictable for simulated convergences <30; however, variability in the data for configurations with simulated convergences between 35 and 40 and a lack of data below a convergence of 35 make conclusions difficult to draw. The plot does show that configurations with simulated convergence >45 are not well predicted by 2D clean Lasnex simulations. Development of a lower convergence, high-performing configuration for MagLIF will help to evaluate the predictive capability of 2D clean Lasnex simulations as a function of convergence.

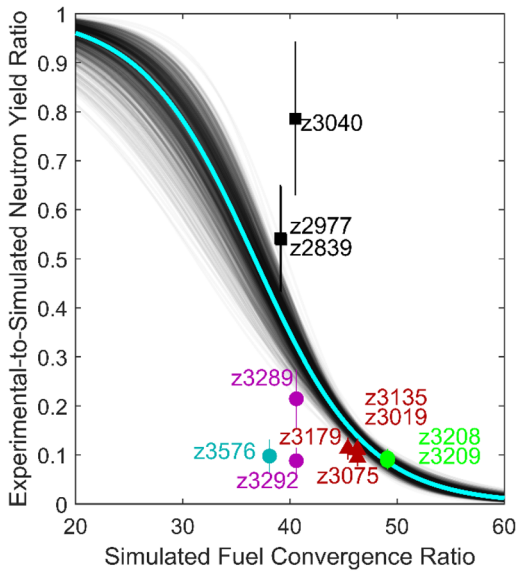

FIG. 12. A plot of the yield over clean as a function of the simulated fuel convergence ratio for the experiments discussed above. Note that z3239 and z3240 were excluded due to abnormal preheat coupling, and z3500 and z3501 were excluded due to significant uncertainty in fuel density. The colors and shapes used to represent the experiments in the plot match those from the plots above to facilitate cross-comparison. Vertical lines represent the 1-σ uncertainty range in the experimental neutron yields. The cyan curve represents a best fit to the data using Eq. (5), and the black curves represent a series of 1000 fits to a Monte Carlo sampling of the uncertainty distributions for the datapoints.

Recent computational efforts using Hydra have captured experimental performance trends in these higher convergence configurations. Hydra simulations in 3D capture the stagnation performance and morphology in MagLIF experiments,[71] but these simulations are computationally expensive and are not used as a design tool. Two-dimensional Hydra simulations in which sufficient axial resolution is included to track instability growth are also able to capture MagLIF experimental performance trends while remaining fast enough to use as an experiment design tool.

IV. DISCUSSION AND SUMMARY

Computational studies[35,50] of the MagLIF concept indicate it has the potential to scale to multi-MJ or even high yield (>200 MJ) at significantly higher current than is achievable on the present-day Z facility. To increase confidence in the identified scaling paths for the MagLIF concept, efforts are being made to study scaling within the range of parameters available at the Z facility. Upgrades to the MagLIF platform have enabled increases in the applied magnetic field, preheat energy, and drive current, with 15 T, 2.3 kJ, and 20 MA simultaneously demonstrated on z3576. The increased range of input parameters enabled experiments with significant increases in neutron production as well as improvements in other stagnation conditions.[113] Up to 3 kJ of preheat energy coupled to the fuel is achievable with the existing ZBL laser, continued development of the 20 T applied magnetic field capability is under way, and optimization of the final transmission line could lead to peak load currents greater than 20 MA for the 10 mm imploding height, AR6 target.

The stagnation performance trends associated with individually changing applied magnetic field, laser preheat energy, and peak load current were studied. Neutron yield and ion temperature increased with applied magnetic field following the trend observed in 2D clean Lasnex simulations. Previous work[17] has shown neutron yield, ion temperature, and fuel magnetization follow the predicted trends with

preheat energy in 2D clean simulations. Here, cryogenics were incorporated into the targets to enable higher preheat energies. Target performance was relatively flat over the space studied, as predicted. LASNEX simulations indicated increased load current would produce significant increases in target performance as well as target convergence. Experiments did not achieve the increased convergence and had similar stagnation performance to lower current targets. When the fuel density, applied magnetic field, and preheat energy were simultaneously increased along with the peak load current, stagnation performance increased, with DD yields as high as 1.1×10^{13} and ion temperatures as high as 3.1 keV.[17] Clean 2D LASNEX simulations of this configuration indicate that the increase in fuel density, axial magnetic field, and preheat energy led to reduced fuel convergence at stagnation. When simulated fuel convergence exceeded 40, experimental performance was significantly degraded relative to simulation performance. Experimental performance may approach 2D clean predictions when the predicted convergence is less than 30, and for this reason, configurations on the simulation-optimized scaling path are designed to maintain a fuel convergence below 30.

In addition to the simulation-optimized efforts to study scaling in MagLIF, efforts to develop a similarity-scaling path to guide choices in the multi-dimensional input parameter space of MagLIF, are under way.[54–56] The goal of these efforts is to develop a scaling path where key physics quantities are preserved in order to increase confidence in projections to a higher current facility. Similar strategies have been applied to laser indirect drive and laser direct drive inertial confinement fusion concepts.[114,115] With the increased range of input parameters available on the Z facility provided by the new MagLIF platform, the proposed similarity-scaling paths can be tested over a wider range, placing greater constraints on the scaling models. Experiments to explore this scaling path are underway.

ACKNOWLEDGMENTS

The authors would like to thank the Z machine, ZBL, and ABZ operations teams, the diagnostics teams, the engineering and CAD teams, and the target fabrication team for their contributions to this work. The work of MRG was partially supported by the Presidential Early Career Award for Scientists and Engineers. Sandia National Laboratories is a multimission laboratory managed and operated by the National Technology and Engineering Solutions of Sandia, LLC, a wholly owned subsidiary of Honeywell International, Inc., for the U.S. Department of Energy's National Nuclear Security Administration under Contract No. DE-NA0003525. General Atomics is funded through the NNSA Target Fabrication Contract No. 89233119CNA000063. This manuscript has been authored in part by Lawrence Livermore National Security, LLC under Contract No. DE-AC52-07NA2 7344 with the US. Department of Energy (LLNL-JRNL-871787). This paper describes objective technical results and analysis. Any subjective views or opinions that might be expressed in the paper do not necessarily represent the views of the U.S. Department of Energy or the U.S. Government. The Publisher acknowledges that the U.S. Government retains a nonexclusive, paid-up, irrevocable, worldwide license to publish or reproduce the published form of this written work or allow others to do so, for U.S. Government purposes. The DOE will provide public access to results of federally sponsored research in accordance with the DOE Public Access Plan.

AUTHOR DECLARATIONS

Conflict of Interest

The authors have no conflicts to disclose.

Author Contributions

Matthew R. Gomez: Conceptualization (lead); Formal analysis (lead); Investigation (equal); Visualization (lead); Writing – original draft (lead). **Stephen A. Slutz:** Conceptualization (supporting); Formal analysis (supporting); Investigation (equal); Writing – review & editing (equal). **Christopher A. Jennings:** Conceptualization (supporting); Formal analysis (supporting); Investigation (equal). **Adam J. Harvey-Thompson:** Conceptualization (supporting); Formal analysis (supporting); Investigation (equal); Project administration (supporting). **Matthew R. Weis:** Conceptualization (supporting); Formal analysis (supporting); Investigation (equal); Writing – review & editing (equal). **William E. Lewis:** Conceptualization (supporting); Formal analysis (supporting); Writing – review & editing (equal). **Brian Hutsel:** Formal analysis (supporting). **Derek Lamppa:** Conceptualization (supporting); Formal analysis (supporting); Investigation (supporting); Writing – review & editing (supporting). **Matthias Geissel:** Conceptualization (supporting); Formal analysis (supporting); Investigation (supporting). **Jerry A. Crabtree:** Conceptualization (supporting); Investigation (supporting). **Thomas J. Awe:** Conceptualization (supporting); Investigation (supporting). **David Yager-Elorriaga:** Conceptualization (supporting); Investigation (supporting). **Daniel E. Ruiz:** Conceptualization (supporting); Investigation (supporting); Writing – review & editing (equal). **Carlos Aragon:** Investigation (supporting). **Kevin A. Benavidez:** Investigation (supporting). **Gordon A. Chandler:** Formal analysis (supporting); Investigation (supporting). **Samuel W. Cordaro:** Conceptualization (supporting). **Jeffrey R. Fein:** Conceptualization (supporting); Investigation (supporting); Writing – review & editing (equal). **Ella S. Field:** Investigation (supporting); Writing – review & editing (equal). **Stephanie B. Hansen:** Conceptualization (supporting); Formal analysis (supporting); Investigation (supporting). **Patrick F. Knapp:** Conceptualization (supporting); Formal analysis (supporting); Investigation (supporting). **Jerry Jackson:** Investigation (supporting). **Ronald J. Kaye:** Investigation (supporting). **Michael Lowinske:** Investigation (supporting). **Larry M. Lucero:** Investigation (supporting). **Clayton E. Myers:** Formal analysis (supporting); Investigation (supporting). **Michael A. Mangan:** Formal analysis (supporting); Investigation (supporting). **Owen M. Mannion:** Conceptualization (supporting); Formal analysis (supporting); Investigation (supporting); Writing – review & editing (equal). **Bryan Norris:** Investigation (supporting). **Reny R. Paguio:** Investigation (supporting); Project administration (supporting). **Lawrence Perea:** Investigation (supporting). **Andrew J. Porwitzky:** Conceptualization (supporting); Formal analysis (supporting); Investigation (supporting). **Patrick K. Rambo:** Investigation (supporting). **Grafton K. Robertson:** Investigation (supporting); Project administration (supporting). **Dean Rovang:** Investigation (supporting). **Fernando Sanchez:** Investigation (supporting). **Mark E. Savage:** Investigation (supporting). **Marc-Andre Schaeuble:** Formal analysis (supporting). **Gabriel A. Shipley:** Conceptualization (supporting); Investigation (supporting). **Jonathon E. Shores:** Investigation (supporting). **Gary Smith:** Investigation (supporting). **Ian Smith:** Investigation (supporting). **C. S. Speas:**

Investigation (supporting). **Jerry Taylor:** Investigation (supporting). **Kurt Tomlinson:** Investigation (supporting). **Kelly A. Whittemore:** Investigation (supporting). **Jeffrey M. Woolstrum:** Conceptualization (supporting); Investigation (supporting). **Edmund P. Yu:** Conceptualization (supporting); Writing – review & editing (equal). **David J. Ampleford:** Conceptualization (supporting); Formal analysis (supporting); Investigation (equal); Project administration (equal); Supervision (equal). **Kristian Beckwith:** Conceptualization (supporting); Project administration (equal); Supervision (equal). **Michael E. Cuneo:** Investigation (supporting); Project administration (supporting). **Eric C. Harding:** Conceptualization (supporting); Formal analysis (supporting); Investigation (equal); Project administration (supporting). **Michael C. Jones:** Investigation (supporting); Project administration (supporting). **Ryan D. McBride:** Conceptualization (supporting); Formal analysis (supporting); Investigation (supporting); Project administration (supporting); Writing – review & editing (equal). **Kyle J. Peterson:** Conceptualization (supporting); Investigation (supporting); Project administration (equal); Supervision (equal). **John L. Porter:** Investigation (supporting); Project administration (supporting). **Gregory A. Rochau:** Conceptualization (supporting); Project administration (supporting); Supervision (equal). **Jens Schwarz:** Investigation (supporting); Project administration (supporting). **Daniel B. Sinars:** Conceptualization (supporting); Investigation (supporting); Project administration (supporting); Supervision (equal); Writing – review & editing (equal).

DATA AVAILABILITY

The data that support the findings of this study are available from the corresponding author upon reasonable request.

REFERENCES

[1]M. Shimada, D. J. Campbell, V. Mukhovatov, M. Fujiwara, N. Kirneva, K. Lackner, M. Nagami, V. D. Pustovitov, N. Uckan, J. Wesley *et al.*, "Progress in the ITER physics basis," Nucl. Fusion **47**, S1 (2007).

[2]R. C. Wolf, C. D. Beidler, A. Dinklage, P. Helander, H. P. Laqua, F. Schauer, T. S. Pedersen, and F. Warmer, "Wendelstein 7-X program—Demonstration of a stellarator option for fusion energy," IEEE Trans. Plasma Sci. **44**, 1466 (2016).

[3]J. H. Nuckolls, L. Wood, A. Thiessen, and G. B. Zimmerman, Nature **239**, 139–142 (1972).

[4]J. Lindl, Phys. Plasmas **2**, 3933 (1995).

[5]A. L. Kritcher, A. B. Zylstra, D. A. Callahan, O. A. Hurricane, C. Weber, J. Ralph, D. T. Casey, A. Pak, K. Baker, B. Bachmann *et al.*, "Achieving record hot spot energies with large HDC implosions on NIF in HYBRID-E," Phys. Plasmas **28**, 072706 (2021).

[6]A. B. Zylstra, O. A. Hurricane, D. A. Callahan, A. L. Kritcher, J. E. Ralph, H. F. Robey, J. S. Ross, C. V. Young, K. L. Baker, D. T. Casey *et al.*, "Burning plasma achieved in inertial fusion," Nature **601**, 542–548 (2022).

[7]I. R. Lindemuth and M. M. Widner, Phys. Fluids **24**, 746 (1981).

[8]I. R. Lindemuth and R. C. Kirkpatrick, Nucl. Fusion **23**, 263 (1983).

[9]A. Hasegawa, H. Daido, M. Fujita, K. Mima, M. Murakami, S. Nakai, K. Nishihara, K. Terai, and C. Yamanaka, Phys. Rev. Lett. **56**(2), 139–142 (1986).

[10]M. M. Basko, A. J. Kemp, and J. Meyer-ter-Vehn, Nucl. Fusion **40**, 59 (2000).

[11]S. A. Slutz, M. C. Herrmann, R. A. Vesey, A. B. Sefkow, D. B. Sinars, D. C. Rovang, K. J. Peterson, and M. E. Cuneo, Phys. Plasmas **17**, 056303 (2010).

[12]S. B. Hansen, M. R. Gomez, A. B. Sefkow, S. A. Slutz, D. B. Sinars, K. D. Hahn, E. C. Harding, P. F. Knapp, P. F. Schmit, T. J. Awe, R. D. McBride, C. A. Jennings, M. Geissel, A. J. Harvey-Thompson, K. J. Peterson, D. C. Rovang, G. A. Chandler, G. W. Cooper, M. E. Cuneo, M. C. Herrmann, M. H. Hess, O. Johns, D. C. Lamppa, M. R. Martin, J. L. Porter, G. K. Robertson, G. A. Rochau, C. L. Ruiz, M. E. Savage, I. C. Smith, W. A. Stygar, R. A. Vesey, B. E. Blue, D. Ryutov, D. G. Schroen, and K. Tomlinson, Phys. Plasmas **22**, 056313 (2015).

[13]P. F. Knapp, M. R. Gomez, S. B. Hansen, M. E. Glinsky, C. A. Jennings, S. A. Slutz, E. C. Harding, K. D. Hahn, M. R. Weis, M. Evans, M. R. Martin, A. J. Harvey-Thompson, M. Geissel, I. C. Smith, D. E. Ruiz, K. J. Peterson, B. M. Jones, J. Schwarz, G. A. Rochau, D. B. Sinars, R. D. McBride, and P.-A. Gourdain, Phys. Plasmas **26**, 012704 (2019).

[14]M. R. Gomez, S. A. Slutz, P. F. Knapp, K. D. Hahn, M. R. Weis, E. C. Harding, M. Geissel, J. R. Fein, M. E. Glinsky, S. B. Hansen, A. J. Harvey-Thompson, C. A. Jennings, I. C. Smith, D. Woodbury, D. J. Ampleford, T. J. Awe, G. A. Chandler, M. H. Hess, D. C. Lamppa, C. E. Myers, C. L. Ruiz, B. Jones, J. L. Porter, K. J. Peterson, R. D. McBride, G. A. Rochau, and D. B. Sinars, IEEE Trans. Plasma Sci. **47**(5), 2081–2101 (2019).

[15]M. R. Gomez, S. A. Slutz, A. B. Sefkow, D. B. Sinars, K. D. Hahn, S. B. Hansen, E. C. Harding, P. F. Knapp, P. F. Schmit, C. A. Jennings, T. J. Awe, M. Geissel, D. C. Rovang, G. A. Chandler, G. W. Cooper, M. E. Cuneo, A. J. Harvey-Thompson, M. C. Herrmann, M. H. Hess, O. Johns, D. C. Lamppa, M. R. Martin, R. D. McBride, K. J. Peterson, J. L. Porter, G. K. Robertson, G. A. Rochau, C. L. Ruiz, M. E. Savage, I. C. Smith, W. A. Stygar, and R. A. Vesey, Phys. Rev. Lett. **113**, 155003 (2014).

[16]M. R. Gomez, S. A. Slutz, A. B. Sefkow, K. D. Hahn, S. B. Hansen, P. F. Knapp, P. F. Schmit, C. L. Ruiz, D. B. Sinars, E. C. Harding, C. A. Jennings, T. J. Awe, M. Geissel, D. C. Rovang, I. C. Smith, G. A. Chandler, G. W. Cooper, M. E. Cuneo, A. J. Harvey-Thompson, M. C. Herrmann, M. H. Hess, D. C. Lamppa, M. R. Martin, R. D. McBride, K. J. Peterson, J. L. Porter, G. A. Rochau, M. E. Savage, D. G. Schroen, W. A. Stygar, and R. A. Vesey, Phys. Plasmas **22**, 056306 (2015).

[17]M. R. Gomez, S. A. Slutz, C. A. Jennings, D. J. Ampleford, M. R. Weis, C. E. Myers, D. A. Yager-Elorriaga, K. D. Hahn, S. B. Hansen, E. C. Harding, A. J. Harvey-Thompson, D. C. Lamppa, M. Mangan, P. F. Knapp, T. J. Awe, G. A. Chandler, G. W. Cooper, J. R. Fein, M. Geissel, M. E. Glinsky, W. E. Lewis, C. L. Ruiz, D. E. Ruiz, M. E. Savage, P. F. Schmit, I. C. Smith, J. D. Styron, J. L. Porter, B. Jones, T. R. Mattsson, K. J. Peterson, G. A. Rochau, and D. B. Sinars, Phys. Rev. Lett. **125**, 155002 (2020).

[18]P. F. Schmit, P. F. Knapp, S. B. Hansen, M. R. Gomez, K. D. Hahn, D. B. Sinars, K. J. Peterson, S. A. Slutz, A. B. Sefkow, T. J. Awe, E. Harding, C. A. Jennings, G. A. Chandler, G. W. Cooper, M. E. Cuneo, M. Geissel, A. J. Harvey-Thompson, M. C. Herrmann, M. H. Hess, O. Johns, D. C. Lamppa, M. R. Martin, R. D. McBride, J. L. Porter, G. K. Robertson, G. A. Rochau, D. C. Rovang, C. L. Ruiz, M. E. Savage, I. C. Smith, W. A. Stygar, and R. A. Vesey, Phys. Rev. Lett. **113**, 155004 (2014).

[19]P. F. Knapp, P. F. Schmit, S. B. Hansen, M. R. Gomez, K. D. Hahn, D. B. Sinars, K. J. Peterson, S. A. Slutz, A. B. Sefkow, T. J. Awe, E. Harding, C. A. Jennings, M. P. Desjarlais, G. A. Chandler, G. W. Cooper, M. E. Cuneo, M. Geissel, A. J. Harvey-Thompson, J. L. Porter, G. A. Rochau, D. C. Rovang, C. L. Ruiz, M. E. Savage, I. C. Smith, W. A. Stygar, and M. C. Herrmann, Phys. Plasmas **22**, 056312 (2015).

[20]W. E. Lewis, P. F. Knapp, S. A. Slutz, P. F. Schmit, G. A. Chandler, M. R. Gomez, A. J. Harvey-Thompson, M. A. Mangan, D. J. Ampleford, and K. Beckwith, "Deep-learning-enables Bayesian inference of fuel magnetization in magnetized liner inertial fusion," Phys. Plasmas **28**, 092701 (2021).

[21]D. C. Rovang, D. C. Lamppa, M. E. Cuneo, A. C. Owen, J. McKenney, D. W. Johnson, S. Radovich, R. J. Kaye, R. D. McBride, C. S. Alexander, T. J. Awe, S. A. Slutz, A. B. Sefkow, T. A. Haill, P. A. Jones, J. W. Argo, D. G. Dalton, G. K. Robertson, E. M. Waisman, D. B. Sinars, J. Meissner, M. Milhous, D. N. Nguyen, and C. H. Mielke, Rev. Sci. Instrum. **85**, 124701 (2014).

[22]P. K. Rambo, I. C. Smith, J. L. Porter, M. J. Hurst, C. S. Speas, R. G. Adams, A. J. Garcia, E. Dawson, B. D. Thurston, C. Wakefield, J. W. Kellogg, M. J. Slattery, H. C. Ives, R. S. Broyles, J. A. Caird, A. C. Erlandson, J. E. Murray, W. C. Behrendt, N. D. Neilsen, and J. M. Narduzzi, J. Appl. Opt. **44**, 12 (2005).

[23]P. K. Rambo, J. Schwarz, M. Schollmeier, M. Geissel, I. Smith, M. Kimmel, C. Speas, J. Shores, D. Armstrong, J. Bellum, E. Field, D. Kletecka, and J. Porter, Proc. SPIE **10014**, 100140Z (2016).

[24]M. E. Savage, K. R. LeChien, M. R. Lopez, B. S. Stoltzfus, W. A. Stygar, D. S. Artery, J. A. Lott, and P. A. Corcoran, "Status of the Z pulsed power driver,"

in *Proceedings of the 18th International Pulsed Power Conference, Chicago, Illinois, 2011* (IEEE, Chicago, Illinois, 2011), pp. 983–990.
[25]D. V. Rose, D. R. Welch, E. A. Madrid, C. L. Miller, R. E. Clark, W. A. Stygar, M. E. Savage, G. A. Rochau, J. E. Bailey, T. J. Nash, M. E. Sceiford, K. W. Struve, P. A. Corcoran, and B. A. Whitney, Phys. Rev. Spec. Top.—Accel. Beams **13**, 010402 (2010).
[26]Values obtained from magnetohydrodynamics simulations in HYDRA.
[27]D. B. Sinars, S. A. Slutz, M. C. Herrmann, R. D. McBride, M. E. Cuneo, K. J. Peterson, R. A. Vesey, C. Nakhleh, B. E. Blue, K. Killebrew, D. Schroen, K. Tomlinson, A. D. Edens, M. R. Lopez, I. C. Smith, J. Shores, V. Bigman, G. R. Bennett, B. W. Atherton, M. Savage, W. A. Stygar, G. T. Leifeste, and J. L. Porter, Phys. Rev. Lett. **105**, 185001 (2010).
[28]D. B. Sinars, S. A. Slutz, M. C. Herrmann, R. D. McBride, M. E. Cuneo, C. A. Jennings, J. P. Chittenden, A. L. Velikovich, K. J. Peterson, R. A. Vesey, C. Nakhleh, E. M. Waisman, B. E. Blue, K. Killebrew, D. Schroen, K. Tomlinson, A. D. Edens, M. R. Lopez, I. C. Smith, J. Shores, V. Bigman, G. R. Bennett, B. W. Atherton, M. Savage, W. A. Stygar, G. T. Leifeste, and J. L. Porter, Phys. Plasmas **18**, 056301 (2011).
[29]R. D. McBride, S. A. Slutz, C. A. Jennings, D. B. Sinars, M. E. Cuneo, M. C. Herrmann, R. W. Lemke, M. R. Martin, R. A. Vesey, K. J. Peterson, A. B. Sefkow, C. Nakhleh, B. E. Blue, K. Killebrew, D. Schroen, T. J. Rogers, A. Laspe, M. R. Lopez, I. C. Smith, B. W. Atherton, M. E. Savage, W. A. Stygar, and J. L. Porter, Phys. Rev. Lett. **109**, 135004 (2012).
[30]R. D. McBride, M. R. Martin, R. W. Lemke, J. B. Greenly, C. A. Jennings, D. C. Rovang, D. B. Sinars, M. E. Cuneo, M. C. Herrmann, S. A. Slutz, C. W. Nakhleh, D. D. Ryutov, J.-P. Davis, D. G. Flicker, B. E. Blue, K. Tomlinson, D. Schroen, R. M. Stamm, G. E. Smith, J. K. Moore, T. J. Rogers, G. K. Robertson, R. J. Kamm, I. C. Smith, M. Savage, W. A. Stygar, G. A. Rochau, M. Jones, M. R. Lopez, J. L. Porter, and M. K. Matzen, Phys. Plasmas **20**, 056309 (2013).
[31]T. J. Awe, R. D. McBride, C. A. Jennings, D. C. Lamppa, M. R. Martin, D. C. Rovang, S. A. Slutz, M. E. Cuneo, A. C. Owen, D. B. Sinars, K. Tomlinson, M. R. Gomez, S. B. Hansen, M. C. Herrmann, J. L. McKenney, C. Nakhleh, G. K. Robertson, G. A. Rochau, M. E. Savage, D. G. Schroen, and W. A. Stygar, Phys. Rev. Lett. **111**, 235005 (2013).
[32]T. J. Awe, C. A. Jennings, R. D. McBride, M. E. Cuneo, D. C. Lamppa, M. R. Martin, D. C. Rovang, D. B. Sinars, S. A. Slutz, A. C. Owen, K. Tomlinson, M. R. Gomez, S. B. Hansen, M. C. Herrmann, M. C. Jones, J. L. McKenney, G. K. Robertson, G. A. Rochau, M. E. Savage, D. G. Schroen, and W. A. Stygar, Phys. Plasmas **21**, 056303 (2014).
[33]E. C. Harding, G. K. Robertson, G. S. Dunham, M. R. Gomez, J. R. Fein, P. F. Knapp, A. J. Harvey-Thompson, C. S. Speas, D. J. Ampleford, G. A. Rochau, R. Doron, and Y. Maron, "X-ray self-emission imaging with spherically bent Bragg crystals on the Z-machine," Rev. Sci. Instrum. **94**, 083509 (2023).
[34]K. R. Carpenter, R. C. Mancini, E. C. Harding, A. J. Harvey-Thompson, M. Geissel, M. R. Weis, S. B. Hansen, K. J. Peterson, and G. A. Rochau, "Magnetic field impact on the laser heating in MagLIF," Phys. Plasmas **27**, 052704 (2020).
[35]S. A. Slutz, M. R. Gomez, S. B. Hansen, E. C. Harding, B. T. Hutsel, P. F. Knapp, D. C. Lamppa, T. J. Awe, D. J. Ampleford, D. E. Bliss, G. A. Chandler, M. E. Cuneo, M. Geissel, M. E. Glinsky, A. J. Harvey-Thompson, M. H. Hess, C. A. Jennings, B. Jones, G. R. Laity, M. R. Martin, K. J. Peterson, J. L. Porter, P. K. Rambo, G. A. Rochau, C. L. Ruiz, M. E. Savage, J. Schwarz, P. F. Schmit, G. Shipley, D. B. Sinars, I. C. Smith, R. A. Vesey, and M. R. Weis, Phys. Plasmas **25**, 112706 (2018).
[36]J. R. Davies, D. H. Barnak, R. Betti, E. M. Campbell, P.-Y. Chang, A. B. Sefkow, K. J. Peterson, D. B. Sinars, and M. R. Weis, "Laser-driven magnetized liner inertial fusion," Phys. Plasmas **24**, 062701 (2017).
[37]D. H. Barnak, J. R. Davies, R. Betti, M. J. Bonino, E. M. Campbell, V. Glebov, D. R. Harding, J. P. Knauer, S. P. Regan, A. B. Sefkow, A. J. Harvey-Thompson, K. J. Peterson, D. B. Sinars, S. A. Slutz, M. R. Weis, and P.-Y. Chang, "Laser-driven magnetized liner inertial fusion on OMEGA," Phys. Plasmas **24**, 056310 (2017).
[38]E. C. Hansen, J. R. Davies, D. H. Barnak, R. Betti, E. M. Campbell, V. Yu. Glebov, J. P. Knauer, L. S. Leal, J. L. Peebles, A. B. Sefkow, and K. M. Woo, "Neutron yield enhancement and suppression by magnetization in laser-driven cylindrical implosions," Phys. Plasmas **27**, 062703 (2020).
[39]L. S. Leal, A. V. Maximov, E. C. Hansen, J. R. Davies, D. H. Barnak, J. L. Peebles, K. M. Woo, P. V. Heuer, A. B. Sefkow, and R. Betti, "Effect of laser preheat in magnetized liner inertial fusion at OMEGA," Phys. Plasmas **29**, 042703 (2022).
[40]J. L. Peebles, J. R. Davies, D. H. Barnak, V. Yu. Glebov, E. C. Hansen, P. V. Heuer, L. S. Leal, M. J. Bonino, D. R. Harding, A. B. Sefkow, K. J. Peterson, D. B. Sinars, E. M. Campbell, and R. Betti, "Demonstration of neutron-yield enhancement by laser preheating and magnetization of laser-driven cylindrical implosions," Phys. Plasmas **30**, 082703 (2023).
[41]See https://www.energy.gov/sites/default/files/2023-11/FY24SSMP_FINAL_NOVEMBER_2023_0.pdf for NNSA, "Fiscal year 2024 Stockpile Stewardship and Management Plan" (2023).
[42]O. A. Hurricane, P. K. Patel, R. Betti, D. H. Froula, S. P. Regan, S. A. Slutz, M. R. Gomez, and M. A. Sweeney, "Physics principles of inertial confinement fusion and U.S. program overview," Rev. Mod. Phys. **95**, 025005 (2023).
[43]H. Abu-Shawareb, R. Acree, P. Adams, J. Adams, B. Addis, R. Aden, P. Adrian, B. B. Afeyan, M. Aggleton, L. Aghaian *et al.* (Indirect Drive ICF Collaboration) "Lawson criterion for ignition exceeded in an inertial fusion experiment," Phys. Rev. Lett. **129**, 075001 (2022).
[44]H. Abu-Shawareb, R. Acree, P. Adams, J. Adams, B. Addis, R. Aden, P. Adrian, B. B. Afeyan, M. Aggleton, L. Aghaian *et al.* (Indirect Drive ICF Collaboration), "Achievement of target gain larger than unity in an inertial fusion experiment," Phys. Rev. Lett. **132**, 065102 (2024).
[45]A. L. Kritcher, D. J. Schlossberg, C. R. Weber, C. V. Young, O. A. Hurricane, E. Dewald, A. B. Zylstra, A. Allen, B. Bachmann, K. L. Baker *et al.*, "Design of first experiment to achieve fusion target gain >1," Phys. Plasmas **31**, 070502 (2024).
[46]G. B. Zimmerman and W. B. Kruer, Comments Plasma Phys. Controlled Fusion **2**, 51 (1975).
[47]B. B. Pollock, C. Goyon, A. B. Sefkow, M. E. Glinsky, K. J. Peterson, M. R. Weis, E. G. Carroll, J. Fry, K. Piston, A. J. Harvey-Thompson, S. B. Hansen, K. Beckwith, D. J. Ampleford, E. R. Tubman, D. J. Strozzi, J. S. Ross, and J. D. Moody, "Experimental demonstration of >20 kJ laser energy coupling in 1-cm hydrocarbon-filled gas pipe targets via inverse Bremsstrahlung absorption with applications to MagLIF," Phys. Plasmas **30**, 022711 (2023).
[48]R. D. McBride and S. A. Slutz, "A semi-analytic model of magnetized liner inertial fusion," Phys. Plasmas **22**, 052708 (2015).
[49]R. D. McBride, S. A. Slutz, R. A. Vesey, M. R. Gomez, A. B. Sefkow, S. B. Hansen, P. F. Knapp, P. F. Schmit, M. Geissel, A. J. Harvey-Thompson, C. A. Jennings, E. C. Harding, T. J. Awe, D. C. Rovang, K. D. Hahn, M. R. Martin, K. R. Cochrane, K. J. Peterson, G. A. Rochau, J. L. Porter, W. A. Stygar, E. M. Campbell, C. W. Nakhleh, M. C. Herrmann, M. E. Cuneo, and D. B. Sinars, "Exploring magnetized liner inertial fusion with a semi-analytic model," Phys. Plasmas **23**, 012705 (2016).
[50]S. A. Slutz, W. A. Stygar, M. R. Gomez, K. J. Peterson, A. B. Sefkow, D. B. Sinars, R. A. Vesey, E. M. Campbell, and R. Betti, Phys. Plasmas **23**, 022702 (2016).
[51]S. A. Slutz and R. A. Vesey, Phys. Rev. Lett. **108**, 025003 (2012).
[52]A. B. Sefkow, S. A. Slutz, J. M. Koning, M. M. Marinak, K. J. Peterson, D. B. Sinars, and R. A. Vesey, Phys. Plasmas **21**, 072711 (2014).
[53]S. A. Slutz, T. J. Awe, and J. A. Crabtree, "Dense hydrogen layers for high performance MagLIF," Phys. Plasmas **29**, 022701 (2022).
[54]P. F. Schmit and D. E. Ruiz, "A conservative approach to scaling magneto-inertial fusion concepts to larger pulsed-power drivers," Phys. Plasmas **27**, 062707 (2020).
[55]D. E. Ruiz, P. F. Schmit, D. A. Yager-Elorriaga, and C. A. Jennings, "Exploring the parameter space of MagLIF implosions using similarity scaling. I. Theoretical framework," Phys. Plasmas **30**, 032707 (2023).
[56]D. E. Ruiz, P. F. Schmit, D. A. Yager-Elorriaga, M. R. Gomez, M. R. Weis, C. A. Jennings, A. J. Harvey-Thompson, P. F. Knapp, S. A. Slutz, D. J. Ampleford, K. Beckwith, and M. K. Matzen, "Exploring the parameter space of MagLIF implosions using similarity scaling. II. Current scaling," Phys. Plasmas **30**, 032708 (2023).
[57]M. M. Marinak, G. D. Kerbel, N. A. Gentile, O. Jones, D. Munro, S. Pollaine, T. R. Dittrich, and S. W. Haan, "Three-dimensional HYDRA simulations of National Ignition Facility targets," Phys. Plasmas **8**, 2275 (2001).

[58]M. M. Marinak, G. B. Zimmerman, T. Chapman, G. D. Kerbal, M. V. Patel, J. M. Koning, S. M. Sepke, B. Chang, C. R. Schroeder, J. A. Harte, D. S. Bailey, L. A. Taylor, S. H. Langer, M. A. Belyaev, D. S. Clark, J. Gaffney, B. A. Hammel, D. E. Hinkel, A. L. Kritcher, J. L. Milovich, H. F. Robey, and C. R. Weber, "How numerical simulations helped to achieve breakeven on the NIF," Phys. Plasmas **31**, 070501 (2024).

[59]Extrapolating the yield curves in Ref. 44, at 12 MA the DD yield would be just below 1×10^{11}. Based on previous experiments, an analyzable DD signal can be recorded on the neutron time of flight detectors at around 1×10^{11}, and at around 4×10^{10} the signal is too weak to obtain a good fit. Indium activation samples have a lower threshold of around 3×10^{9} but an nTOF signal is needed to confirm that neutrons are the source of the signal since high energy photons from the pulsed power driver can also contribute to the signal. Similarly, x-ray diode and x-ray self-emission imager signals are observed to rise above the noise floor on those diagnostics when the target produces between 1×10^{10} and 1×10^{11} DD neutrons.

[60]The first three MagLIF experiments were conducted with 7.5 mm tall imploding regions, and approximately 18 MA was delivered to those targets. Nearly all subsequent MagLIF experiments have been conducted with 10 mm tall imploding regions with approximately 16 MA delivered to the load.

[61]C. A. Jennings, J. P. Chittenden, M. E. Cuneo, W. A. Stygar, D. J. Ampleford, E. M. Waisman, M. Jones, M. E. Savage, K. R. LeChien, and T. C. Wagoner, "Circuit modeling for driving three-dimensional resistive MHD wire array Z-pinch calculations," IEEE Trans. Plasma Sci. **38**, 529–539 (2010).

[62]A. Porwitzky and J. Brown, "Accounting for slotted cylindrical anodes in current inferences on pulsed power drivers," in *Proceedings of the 2018 IEEE International Power Modulator and High Voltage Conference*, Jackson, WY (IEEE, 2018), pp. 128–132.

[63]A. Porwitzky and J. Brown, "Uncertainties in cylindrical anode current inferences on pulsed power drivers," Phys. Plasmas **25**, 063102 (2018).

[64]D. V. Rose, D. R. Welch, T. P. Hughes, R. E. Clark, and W. A. Stygar, Phys. Rev. Spec. Top.—Accel. Beams **11**, 060401 (2008).

[65]E. A. Madrid, D. V. Rose, D. R. Welch, R. E. Clark, C. B. Mostrom, W. A. Stygar, M. E. Cuneo, M. R. Gomez, T. P. Hughes, T. D. Pointon, and D. B. Seidel, Phys. Rev. Spec. Top.—Accel. Beams **16**, 120401 (2013). [Database][Mismatch

[66]D. V. Rose, E. A. Madrid, D. R. Welch, R. E. Clark, C. B. Mostrom, W. A. Stygar, and M. E. Cuneo, Phys. Rev. Spec. Top.—Accel. Beams **18**, 030402 (2015).

[67]M. R. Gomez, R. M. Gilgenbach, M. E. Cuneo, C. A. Jennings, R. D. McBride, E. M. Waisman, B. T. Hutsel, W. A. Stygar, D. V. Rose, and Y. Maron, Phys. Rev. Accel. Beams **20**, 010401 (2017).

[68]N. Bennett, D. R. Welch, K. Cochrane, K. Leung, C. Thoma, M. E. Cuneo, and G. Frye-Mason, "Electrode plasma formation and melt in Z-pinch accelerators," Phys. Rev. Accel. Beams **26**, 040401 (2023).

[69]The reported uncertainties in the inductance for both the load volume and the final transmission line are due to variability in the axial separation of the anode and cathode in the final transmission line. The axial location of the anode relative to the cathode can vary by +/− 0.064 mm, resulting in a slightly larger or smaller inductive volume. Manufacturing tolerances on machined parts will also contribute to the inductance uncertainty but were ignored for this estimate.

[70]B. T. Hutsel, P. A. Corcoran, M. E. Cuneo, M. R. Gomez, M. H. Hess, D. D. Hinshelwood, C. A. Jennings, G. R. Laity, D. C. Lamppa, R. D. McBride, J. K. Moore, A. Myers, D. V. Rose, S. A. Slutz, W. A. Stygar, E. M. Waisman, D. R. Welch, and B. A. Whitney, Phys. Rev. Accel. Beams **21**, 030401 (2018).

[71]M. R. Weis, D. E. Ruiz, M. R. Gomez, A. J. Harvey-Thompson, C. A. Jennings, D. A. Yager-Elorriaga, W. E. Lewis, S. A. Slutz, L. N. Shulenburger, and D. J. Ampleford, "Assessing the performance of MagLIF with 3D MHD simulation" Phys. Plasmas **32**, 022708 (2025).

[72]O. A. Hurricane, "Optimized minimal inductance transmission line configuration for Z-pinch experiments," J. Appl. Phys. **95**, 4503 (2004).

[73]E. M. Waisman and M. E. Cuneo, "Minimal inductance for axisymmetric transmission lines with radially dependent anode-cathode gap," Phys. Rev. Spec. Top.—Accel. Beams **12**, 090401 (2009).

[74]A. C. Robinson and C. J. Garasi, "Three-dimensional Z-pinch wire array modeling with ALEGRA-HEDP," Comput. Phys. Commun. **164**, 408–413 (2004).

[75]W. E. Lewis, D. A. Yager-Elorriaga, C. A. Jennings, J. R. Fein, G. A. Shipley, A. Porwitzky, T. J. Awe, M. R. Gomez, E. C. Harding, A. J. Harvey-Thompson, P. F. Knapp, O. M. Mannion, D. E. Ruiz, M.-A. Schaeuble, S. A. Slutz, M. R. Weis, J. Woolstrum, D. J. Ampleford, and L. Shulenburger, "Mining experimental magnetized liner inertial fusion data: Trends in stagnation morphology," Phys. Plasmas **31**, 082710 (2024).

[76]P. W. Lake, J. E. Bailey, G. A. Rochau, T. C. Moore, D. Petmecky, and P. Gard, "Time- and space-resolved elliptical crystal spectrometers for high energy density physics research," Rev. Sci. Instrum **75**(10), 3690–3692 (2004).

[77]B. Jones, C. Deeney, C. A. Coverdale, C. J. Meyer, and P. D. LePell, "Monochromatic x-ray self-emission imaging of imploding wire array Z-pinches on the Z accelerator," IEEE Trans. Plasma Sci. **34**(2), 213–222 (2006).

[78]M. C. Jones, D. J. Ampleford, M. E. Cuneo, R. Hohlfelder, C. A. Jennings, D. W. Johnson, B. Jones, M. R. Lopez, J. MacArthur, J. A. Mills, T. Preston, G. A. Rochau, M. Savage, D. Spencer, D. B. Sinars, and J. L. Porter, "X-ray power and yield measurements at the refurbished Z machine," Rev. Sci. Instrum. **85**, 083501 (2014).

[79]E. C. Harding, T. Ao, J. E. Bailey, G. Loisel, D. B. Sinars, M. Geissel, G. A. Rochau, and I. C. Smith, "Analysis and implementation of a space resolving spherical crystal spectrometer for x-ray Thomson scattering experiments," Rev. Sci. Instrum. **86**, 043504 (2015).

[80]L. A. McPherson, D. J. Ampleford, C. A. Coverdale, J. W. Argo, A. C. Owen, and D. M. Jaramillo, "High energy X-ray pinhole Imaging at the Z facility," Rev. Sci. Instrum. **87**, 063502 (2016).

[81]D. J. Ampleford, C. L. Ruiz, D. N. Fittinghoff, J. D. Vaughan, K. Hahn, B. Lahmann, M. Gatu-Johnson, J. Frenje, R. Petrasso, C. R. Ball, A. J. Maurer, P. F. Knapp, A. J. Harvey-Thompson, J. Fisher, P. Alberto, J. A. Torres, G. Cooper, B. Jones, G. A. Rochau, and M. J. May, "One dimensional imager of neutrons on the Z machine," Rev. Sci. Instrum. **89**, 10I132 (2018).

[82]T. J. Webb, D. Ampleford, C. R. Ball, M. R. Gomez, P. W. Lake, A. Maurer, and R. Presura, "A time-resolved, in-chamber x-ray pinhole imager for Z," Rev. Sci. Instrum. **92**, 033512 (2021).

[83]D. C. Lamppa, "Advanced electromagnet designs enabling 15-20 T axial fields in 20 MA magnetized liner inertial fusion experiments," unpublished (2025).

[84]S. A. Slutz, C. A. Jennings, T. J. Awe, G. A. Shipley, B. T. Hutsel, and D. C. Lamppa, "Auto-magnetizing liners for magnetized inertial fusion," Phys. Plasmas **24**, 012704 (2017).

[85]G. A. Shipley, T. J. Awe, B. T. Hutsel, J. B. Greenly, C. A. Jennings, and S. A. Slutz, "Implosion of auto-magnetizing helical liners on the Z facility," Phys. Plasmas **26**, 052705 (2019).

[86]P. C. Campbell, T. M. Jones, J. M. Woolstrum, N. M. Jordan, P. F. Schmit, A. L. Velikovich, J. B. Greenly, W. M. Potter, E. S. Lavine, B. R. Kusse, D. A. Hammer, and R. D. McBride, "Liner implosion experiments driven by a dynamic screw pinch," Phys. Plasmas **28**, 082707 (2021).

[87]D. Zimmer, M. R. Gomez, N. Bennett, C. A. Jennings, C. E. Myers, D. C. Lamppa, F. Conti, and F. N. Beg, "Understanding the impact of an applied magnetic field on efficient current coupling on the Z machine," Phys. Rev. Accel. Beams **27**, 100401 (2024).

[88]D. J. Armstrong, Q. M. Looker, J. W. Stahoviak, I. C. Smith, J. E. Shores, P. K. Rambo, J. Schwarz, C. S. Speas, and J. L. Porter, Rev. Sci. Instrum. **89**, 105106 (2018).

[89]M. Geissel, T. J. Awe, D. E. Bliss, M. E. Campbell, M. R. Gomez, E. Harding, A. J. Harvey-Thompson, S. B. Hansen, C. Jennings, M. W. Kimmel, P. Knapp, S. M. Lewis, R. D. McBride, K. Peterson, M. Schollmeier, D. J. Scoglietti, A. B. Sefkow, J. E. Shores, D. B. Sinars, S. A. Slutz, I. C. Smith, C. S. Speas, R. A. Vesey, and J. L. Porter, Proc. SPIE **9731**, 97310O (2016).

[90]M. Geissel, A. J. Harvey-Thompson, T. J. Awe, D. E. Bliss, M. E. Glinsky, M. R. Gomez, E. Harding, S. B. Hansen, C. Jennings, M. W. Kimmel, P. Knapp, S. M. Lewis, K. Peterson, M. Schollmeier, J. Schwarz, J. E. Shores, S. A. Slutz, D. B. Sinars, I. C. Smith, C. S. Speas, R. A. Vesey, M. R. Weis, and J. L. Porter, Phys. Plasmas **25**, 022706 (2018).

[91]S. M. Miller, S. A. Slutz, S. N. Bland, S. R. Klein, P. C. Campbell, J. M. Woolstrum, C. C. Kuranz, M. R. Gomez, N. M. Jordan, and R. D. McBride, "A pulsed-power implementation of laser gate for increasing laser energy coupling and fusion yield in magnetized liner inertial fusion (MagLIF)," Rev. Sci. Instrum. **91**, 063507 (2020).

[92]B. R. Galloway, S. A. Slutz, M. W. Kimmel, P. K. Rambo, J. Schwarz, M. Geissel, A. J. Harvey-Thompson, M. R. Weis, C. A. Jennings, E. S. Field, D. E. Kletecka, Q. Looker, A. P. Colombo, A. D. Edens, I. C. Smith, J. E. Shores, C. S. Speas, R. J. Speas, A. P. Spann, J. Sin, S. Gautier, V. Sauget, P. A. Treadwell, G. A. Rochau, and J. L. Porter, "Lasergate: A windowless gas target for enhanced laser preheat in magnetized liner inertial fusion," Phys. Plasmas **28**, 112703 (2021).
[93]A. J. Harvey-Thompson, M. Geissel, J. A. Crabtree, M. R. Weis, M. R. Gomez, J. R. Fein, W. E. Lewis, D. J. Ampleford, T. J. Awe, G. A. Chandler, B. R. Galloway, S. B. Hansen, J. Hanson, E. C. Harding, C. A. Jennings, M. Kimmel, P. F. Knapp, M. A. Mangan, A. Maurer, R. R. Paguio, L. Perea, K. J. Peterson, J. L. Porter, P. K. Rambo, G. K. Robertson, G. A. Rochau, D. E. Ruiz, J. E. Shores, S. A. Slutz, G. E. Smith, I. C. Smith, C. S. Speas, D. A. Yager-Elorriaga, and A. York, "Demonstration of improved laser preheat with a cryogenically-cooled magnetized liner inertial fusion platform," Rev. Sci. Instrum. **94**, 053506 (2023).
[94]M. R. Weis, A. J. Harvey-Thompson, and D. E. Ruiz, "Scaling laser preheat for MagLIF with the Z-Beamlet laser," Phys. Plasmas **28**, 012705 (2021).
[95]D. J. Ampleford, D. A. Yager-Elorriaga, C. A. Jennings, E. C. Harding, M. R. Gomez, A. J. Harvey-Thompson, T. J. Awe, G. A. Chandler, G. S. Dunham, M. Geissel *et al.*, "Controlling morphology and improving reproducibility of magnetized liner inertial fusion experiments," Phys. Plasmas **31**, 022703 (2024).
[96]K. J. Peterson, T. J. Awe, E. P. Yu, D. B. Sinars, E. S. Field, M. E. Cuneo, M. C. Herrmann, M. Savage, D. Schroen, K. Tomlinson, and C. Nakhleh, Phys. Rev. Lett. **112**, 135002 (2014).
[97]T. J. Awe, K. J. Peterson, E. P. Yu, R. D. McBride, D. B. Sinars, M. R. Gomez, C. A. Jennings, M. R. Martin, S. E. Rosenthal, D. G. Schroen, A. B. Sefkow, S. A. Slutz, K. Tomlinson, and R. A. Vesey, Phys. Rev. Lett. **116**, 065001 (2016).
[98]A. J. Harvey-Thompson, M. E. Geissel, W. E. Lewis, D. A. Yager-Elorriaga, M. R. Weis, C. A. Jennings, J. R. Fein, D. J. Ampleford, M. R. Gomez, E. C. Harding, S. B. Hansen, D. E. Bliss, G. A. Chandler, G. S. Dunham, E. S. Field, B. R. Galloway, M. Glinsky, K. D. Hahn, P. F. Knapp, D. C. Lamppa, L. M. Lucero, M. A. Mangan, R. R. Paguio, L. Perea, K. J. Peterson, J. L. Porter, P. K. Rambo, G. K. Robertson, G. A. Rochau, D. E. Ruiz, C. L. Ruiz, M. A. Schaeuble, J. Schwarz, J. E. Shores, D. B. Sinars, S. A. Slutz, G. E. Smith, I. C. Smith, C. S. Speas, K. Whittemore, and E. P. Yu, "Development of a high performance MagLIF target platform using high aspect ratio coated liners and low-mix laser preheat," Phys. Plasmas **31**, 072711 (2024).
[99]V. I. Oreshkin, R. B. Baksht, N. A. Ratakhin, A. V. Shishlov, K. V. Khishchenko, P. R. Levashov, and I. I. Beilis, Phys. Plasmas **11**, 4771 (2004).
[100]K. J. Peterson, D. B. Sinars, E. P. Yu, M. C. Herrmann, M. E. Cuneo, S. A. Slutz, I. C. Smith, B. W. Atherton, M. D. Knudson, and C. Nakhleh, Phys. Plasmas **19**, 092701 (2012).
[101]E. P. Yu, T. J. awe, K. R. Cochrane, K. C. Yates, T. M. Hutchinson, K. J. Peterson, and B. S. Bauer, Phys. Plasmas **27**, 052703 (2020).
[102]E. P. Yu, T. J. Awe, K. R. Cochrane, K. J. Peterson, K. C. Yates, T. M. Hutchinson, M. W. Hatch, B. S. Bauer, K. Tomlinson, and D. B. Sinars, Phys. Rev. Lett. **130**, 255101 (2023).
[103]P. F. Schmit, A. L. Velikovich, R. D. McBride, and G. K. Robertson, "Controlling Rayleigh–Taylor instabilities in magnetically driven solid metal shells by means of a dynamic screw pinch," Phys. Rev. Lett. **117**, 205001 (2016).
[104]G. A. Shipley, C. A. Jennings, and P. F. Schmit, "Design of dynamic screw pinch experiments for magnetized liner inertial fusion," Phys. Plasmas **26**, 102702 (2019).
[105]P. C. Campbell, T. M. Jones, J. M. Woolstrum, N. M. Jordan, P. F. Schmit, J. B. Greenly, W. M. Potter, E. S. Lavine, B. R. Kusse, D. A. Hammer, and R. D. McBride, "Stabilization of liner implosions via a dynamic screw pinch," Phys. Rev. Lett. **125**, 035001 (2020).
[106]G. A. Chandler, C. L. Ruiz, G. W. Cooper, J. A. Torres, M. A. Mangan, G. M. Whitlow, D. J. Ampleford, M. C. Jones, R. A. Buckles, K. J. Moy, I. Garza, M. Staska, A. Wolverton, and B. Davis, "Neutron time-of-flight detectors (nTOF) used at Sandia's Z-machine," Rev. Sci. Instrum. **93**(11), 113531 (2022).
[107]A. J. Harvey-Thompson, M. Geissel, C. A. Jennings, M. R. Weis, M. R. Gomez, J. R. Fein, D. J. Ampleford, G. A. Chandler, M. E. Glinsky, K. D. Hahn, S. B. Hansen, E. C. Harding, P. F. Knapp, R. R. Paguio, L. Perea, K. J. Peterson, J. L. Porter, P. K. Rambo, G. K. Robertson, G. A. Rochau, C. L. Ruiz, J. Schwarz, J. E. Shores, D. B. Sinars, S. A. Slutz, G. E. Smith, I. C. Smith, C. S. Speas, K. Whittemore, and D. Woodbury, Phys. Plasmas **26**, 032707 (2019).
[108]T. J. Awe, K. P. Shelton, A. B. Sefkow, D. C. Lamppa, J. L. Baker, D. C. Rovang, and G. K. Robertson, "Development of a cryogenically cooled platform for the Magnetized Liner Inertial Fusion (MagLIF) Program," Rev. Sci. Instrum. **88**, 093515 (2017).
[109]J. M. Woolstrum, C. E. Seyler, and R. D. McBride, "Hall instability driven seeding of helical magneto-Rayleigh-Taylor instabilities in axially premagnetized thin-foil liner Z-pinch implosions," Phys. Plasmas **29**, 122701 (2022).
[110]M. H. Hess, K. J. Peterson, D. J. Ampleford, B. T. Hutsel, C. A. Jennings, M. R. Gomez, D. H. Dolan, G. K. Robertson, S. L. Payne, W. A. Stygar, M. R. Martin, and D. B. Sinars, "Design and testing of a magnetically driven implosion peak current diagnostic," Phys. Plasmas **25**, 042702 (2018).
[111]R. E. Olson, R. J. Leeper, J. L. Kline, A. B. Zylstra, S. A. Yi, J. Biener, T. Braun, B. J. Kozioziemski, J. D. Sater, P. A. Bradley *et al.*, "First liquid layer inertial confinement fusion implosions at the National Ignition Facility," Phys. Rev. Lett. **117**, 245001 (2016).
[112]S. P. Regan, V. N. Goncharov, I. V. Igumenshchev, T. C. Sangster, R. Betti, A. Bose, T. R. Boehly, M. J. Bonino, E. M. Campbell, D. Cao *et al.*, "Demonstration of fuel hot-spot pressure in excess of 50 Gbar for direct-drive, layered deuterium-tritium implosions on OMEGA," Phys. Rev. Lett. **117**, 025001 (2016).
[113]P. F. Knapp, M. E. Glinsky, M. A. Schaeuble, C. A. Jennings, M. Evans, J. Gunning, T. J. Awe, G. A. Chandler, M. Geissel, M. R. Gomez, K. D. Hahn, S. B. Hansen, E. C. Harding, A. J. Harvey-Thompson, S. Humane, B. T. Klein, M. Mangan, T. Nagayama, A. J. Porwitzky, D. E. Ruiz, P. F. Schmit, S. A. Slutz, I. C. Smith, M. R. Weis, D. A. Yager-Elorriaga, D. J. Ampleford, K. Beckwith, T. R. Mattsson, K. J. Peterson, and D. B. Sinars, "Estimation of stagnation performance metrics in magnetized liner inertial fusion experiments using Bayesian data assimilation," Phys. Plasmas **29**, 052711 (2022).
[114]R. Nora, R. Betti, K. S. Anderson, A. Shvydky, A. Bose, K. M. Woo, A. R. Christopherson, J. A. Marozas, T. J. B. Collins, P. B. Radha, S. X. Hu, R. Epstein, F. J. Marshall, R. L. McCrory, T. C. Sangster, and D. D. Meyerhofer, "Theory of hydro-equivalent ignition for inertial fusion and its applications to OMEGA and the National Ignition Facility," Phys. Plasmas **21**, 056316 (2014).
[115]K. L. Baker, O. Jones, C. Weber, D. Clark, P. K. Patel, C. A. Thomas, O. L. Landen, R. Nora, G. J. Anderson, J. Gaffney, S. MacLaren, D. T. Casey, T. Doppner, E. L. Dewald, R. Tommasini, B. K. Spears, J. Salmonson, M. Hohenberger, S. Khan, A. Zylstra, A. Kritcher, P. Amendt, V. Smalyuk, J. Lindl, C. Young, J. S. Ross, D. Ho, O. A. Hurricane, D. A. Callahan, T. Woods, J. L. Milovich, D. J. Strozzi, B. Bachmann, R. Bionta, P. M. Celliers, D. Fittinghoff, R. Hatarik, M. Gatu Johnson, K. Meaney, M. Millot, P. L. Volegov, and C. Wilde, "Hydroscaling indirect-drive implosions on the National Ignition Facility," Phys. Plasmas **29**, 062705 (2022).